UNIVERSITY OF BIRMINGHAM

University of Birmingham
Research at Birmingham

Signatures of magnetic activity in the seismic data of solar-type stars observed by Kepler

Santos, A. R. G.; Campante, T. L.; Chaplin, W. J.; Cunha, M. S.; Lund, M. N.; Kiefer, R.; Salabert, D.; Garcia, R. A.; Davies, G. R.; Elsworth, Y; Howe, R.

Document Version
Publisher's PDF, also known as Version of record

Link to publication on Research at Birmingham portal

Signatures of Magnetic Activity in the Seismic Data of Solar-type Stars Observed by *Kepler*

A. R. G. Santos[1,2,3,4] , T. L. Campante[2,3,4] , W. J. Chaplin[4,5] , M. S. Cunha[2,3] , M. N. Lund[4,5] , R. Kiefer[6] ,
D. Salabert[7,8] , R. A. García[7,8], G. R. Davies[4,5] , Y. Elsworth[4,5], and R. Howe[4,5]

[1] Space Science Institute, 4750 Walnut Street, Suite 205, Boulder CO 80301, USA; asantos@spacescience.org
[2] Instituto de Astrofísica e Ciências do Espaço, Universidade do Porto, CAUP, Rua das Estrelas, PT-4150-762 Porto, Portugal
[3] Departamento de Física e Astronomia, Faculdade de Ciências, Universidade do Porto, Rua do Campo Alegre 687, PT-4169-007 Porto, Portugal
[4] School of Physics and Astronomy, University of Birmingham, Edgbaston, Birmingham B15 2TT, UK
[5] Stellar Astrophysics Centre, Department of Physics and Astronomy, Aarhus University, Ny Munkegade 120, DK-8000 Aarhus C, Denmark
[6] Kiepenheuer-Institut für Sonnenphysik, Schöneckstraße 6, D-79104 Freiburg, Germany
[7] IRFU, CEA, Université Paris-Saclay, F-91191 Gif-sur-Yvette, France
[8] Université Paris Diderot, AIM, Sorbonne Paris Cité, CEA, CNRS, F-91191 Gif-sur-Yvette, France
Received 2018 January 2; revised 2018 May 24; accepted 2018 May 28; published 2018 July 19

Abstract

In the Sun, the frequencies of the acoustic modes are observed to vary in phase with the magnetic activity level. These frequency variations are expected to be common in solar-type stars and contain information about the activity-related changes that take place in their interiors. The unprecedented duration of *Kepler* photometric time-series provides a unique opportunity to detect and characterize stellar magnetic cycles through asteroseismology. In this work, we analyze a sample of 87 solar-type stars, measuring their temporal frequency shifts over segments of 90 days. For each segment, the individual frequencies are obtained through a Bayesian peak-bagging tool. The mean frequency shifts are then computed and compared with: (1) those obtained from a cross-correlation method; (2) the variation in the mode heights; (3) a photometric activity proxy; and (4) the characteristic timescale of the granulation. For each star and 90-day sub-series, we provide mean frequency shifts, mode heights, and characteristic timescales of the granulation. Interestingly, more than 60% of the stars show evidence for (quasi-)periodic variations in the frequency shifts. In the majority of the cases, these variations are accompanied by variations in other activity proxies. About 20% of the stars show mode frequencies and heights varying approximately in phase, in opposition to what is observed for the Sun.

Key words: asteroseismology – methods: data analysis – stars: activity – stars: oscillations – stars: solar-type

Supporting material: figure set, machine-readable table

1. Introduction

Solar-type pulsators, such as low-mass main-sequence stars, exhibit acoustic oscillations (p-modes) that are stochastically excited by near-surface convection (e.g., Goldreich & Keeley 1977). Furthermore, convection, together with stellar differential rotation, also plays an important role in the generation of magnetic fields and activity cycles (e.g., Brun & Browning 2017).

As the magnetic fields affect the medium where the acoustic waves propagate, the p-modes are sensitive to changes in the magnetic activity. In the Sun, the mode frequencies and the damping rates are observed to vary in phase with the activity level, while the mode amplitudes vary in anti-phase (e.g., Woodard & Noyes 1985; Elsworth et al. 1990; Libbrecht & Woodard 1990; Chaplin et al. 1998; Howe et al. 2015). Although the frequency shifts are found to be well correlated with other activity indicators (e.g., 10.7 cm flux, sunspot number, sunspot area, magnetic plage strength index, photometric activity proxy) over the solar cycle (e.g., Chaplin et al. 2007; Tripathy et al. 2007; Jain et al. 2009; Broomhall & Nakariakov 2015; Santos et al. 2016, 2017; Salabert et al. 2017), they also show a temporal offset (being ahead in time) in relation to those activity proxies (e.g., Jiménez-Reyes et al. 1998; Moreno-Insertis & Solanki 2000; Jain et al. 2009; Salabert et al. 2009, 2015).

In addition to the long-term variation on the timescale of the 11-year solar cycle, the mode frequencies also vary on a quasi-biennial timescale (e.g., Fletcher et al. 2010; Broomhall et al. 2012; Simoniello et al. 2012, 2013; Broomhall & Nakariakov 2015; Salabert et al. 2015). The quasi-biennial signal is present in all phases of activity, and is modulated by the 11-year cycle, i.e., it has its largest amplitudes around the solar maximum. Quasi-biennial variations are also detected in other solar phenomena and activity indicators, such as sunspot number and area coverage, flare and coronal mass ejection rates, total and spectral solar irradiance, 10.7 cm flux, and photometric activity proxy $S_{\rm ph}$ (e.g., Bazilevskaya et al. 2014; McIntosh et al. 2015; Salabert et al. 2017). In fact, these mid-term variations are found to be strongly correlated with those in the solar acoustic frequencies (Broomhall et al. 2012; Broomhall & Nakariakov 2015).

Multiple periodicities in the magnetic activity level, measured from chromospheric and photometric proxies, are also observed in several solar-type stars (e.g., Baliunas et al. 1995; Oláh et al. 2009; Metcalfe et al. 2010, 2013; Egeland et al. 2015; Flores et al. 2017). Similar to the solar case, for some of those stars, the longer cycle seems to modulate the shorter cycle (Oláh et al. 2009; Metcalfe et al. 2013).

These activity-related changes in the seismic properties are also expected to be common among solar-type stars. The first seismic detection of such a signature in a star other than the Sun was made by García et al. (2010). The authors found evidence for an activity cycle in the photometric and seismic

Table 1
Stellar Parameters of the Target Sample Composed of 87 *Kepler* Solar-type Stars

| KIC	KOI	Kp	Quarters	ν_{max} (μHz)	$\Delta\nu$ (μHz)	T_{eff} (K)	[Fe/H] (dex)	log g (dex)	P_{rot} (days)
1435467	$\cdots$	8.88	Q5.1–Q17.2	$1406.7^{+6.3}_{-8.4}$	$70.369^{+0.034}_{-0.033}$	6326 ± 77 (1)	0.01 ± 0.1 (1)	$4.100^{+0.009}_{-0.009}$	6.68 ± 0.89 (9)
2837475	$\cdots$	8.48	Q5.1–Q17.2	$1557.6^{+8.2}_{-9.2}$	$75.729^{+0.041}_{-0.042}$	6614 ± 77 (1)	0.01 ± 0.1 (1)	$4.163^{+0.007}_{-0.007}$	3.68 ± 0.36 (9)
3425851	268	10.56	Q6.1–Q8.3	$2038.0^{+60.0}_{-60.0}$	$92.600^{+2.500}_{-2.500}$	6343 ± 85 (2)	-0.04 ± 0.1 (2)	$4.243^{+0.008}_{-0.008}$	7.873 ± 0.001 (10)
3427720	$\cdots$	9.11	Q5.1–Q17.2	$2737.0^{+10.7}_{-17.7}$	$120.068^{+0.031}_{-0.032}$	6045 ± 77 (1)	-0.06 ± 0.1 (1)	$4.387^{+0.004}_{-0.005}$	13.94 ± 2.15 (11)
3456181	$\cdots$	9.66	Q5.1–Q11.3	$970.0^{+8.3}_{-5.9}$	$52.264^{+0.041}_{-0.039}$	6384 ± 77 (1)	-0.15 ± 0.1 (1)	$3.950^{+0.005}_{-0.007}$	$\cdots$
3544595	69	9.93	Q2.3–Q17.2	$3366.0^{+81.0}_{-81.0}$	$147.770^{+0.450}_{-0.450}$	5669 ± 75 (2)	-0.18 ± 0.1 (2)	$4.468^{+0.003}_{-0.003}$	$\cdots$
3632418	975	8.22	Q5.1–Q17.2	$1166.8^{+3.0}_{-3.8}$	$60.704^{+0.019}_{-0.018}$	6193 ± 77 (1)	-0.12 ± 3.0 (1)	$4.024^{+0.005}_{-0.007}$	12.591 ± 0.036 (10)
3656476	$\cdots$	9.52	Q5.1–Q17.2	$1925.0^{+7.0}_{-6.3}$	$93.194^{+0.018}_{-0.020}$	5668 ± 77 (1)	0.25 ± 0.1 (1)	$4.225^{+0.010}_{-0.008}$	31.67 ± 3.53 (9)
3735871	$\cdots$	9.71	Q5.1–Q17.2	$2862.6^{+16.6}_{-26.5}$	$123.049^{+0.047}_{-0.046}$	6107 ± 77 (1)	-0.04 ± 0.1 (1)	$4.396^{+0.007}_{-0.007}$	11.53 ± 1.24 (9)
4141376	280	11.07	Q6.1–Q17.2	$2928.0^{+97.0}_{-97.0}$	$128.800^{+1.300}_{-1.300}$	6134 ± 91 (2)	-0.24 ± 0.1 (2)	$4.412^{+0.003}_{-0.004}$	15.78 ± 2.12 (12)
4349452	244	10.73	Q5.1–Q17.2	$2106.0^{+50.0}_{-50.0}$	$98.270^{+0.570}_{-0.570}$	6270 ± 79 (2)	-0.04 ± 0.1 (2)	$4.275^{+0.007}_{-0.008}$	23.147 ± 0.039 (10)
4914423	108	12.29	Q3.1–Q12.3	$1663.0^{+56.0}_{-56.0}$	$81.500^{+1.600}_{-1.600}$	5845 ± 88 (2)	0.07 ± 0.11 (2)	$4.155^{+0.009}_{-0.009}$	$\cdots$
4914923	$\cdots$	9.46	Q5.1–Q17.2	$1817.0^{+6.3}_{-5.2}$	$88.531^{+0.019}_{-0.019}$	5805 ± 77 (1)	0.08 ± 0.1 (1)	$4.197^{+0.010}_{-0.008}$	20.49 ± 2.82 (9)
5184732	$\cdots$	8.16	Q7.1–Q17.2	$2089.3^{+4.4}_{-4.1}$	$95.545^{+0.024}_{-0.023}$	5846 ± 77 (1)	0.36 ± 0.1 (1)	$4.255^{+0.008}_{-0.010}$	19.79 ± 2.43 (9)
5773345	$\cdots$	9.16	Q6.1–Q11.3	$1101.2^{+5.7}_{-6.6}$	$57.303^{+0.030}_{-0.027}$	6130 ± 84 (3)	0.21 ± 0.09 (3)	$3.993^{+0.007}_{-0.007}$	11.57 ± 1.02 (9)
5866724	85	11.02	Q3.1–Q17.2	$1880.0^{+60.0}_{-60.0}$	$89.560^{+0.480}_{-0.480}$	6169 ± 50 (2)	0.09 ± 0.08 (2)	$4.224^{+0.005}_{-0.007}$	7.911 ± 0.155 (10)
5950854	$\cdots$	10.96	Q5.1–Q10.3	$1926.7^{+21.9}_{-20.4}$	$96.629^{+0.102}_{-0.107}$	5853 ± 77 (1)	-0.23 ± 0.1 (1)	$4.238^{+0.007}_{-0.007}$	$\cdots$
6106415	$\cdots$	7.18	Q6.1–Q16.3	$2248.6^{+4.6}_{-3.9}$	$104.074^{+0.023}_{-0.026}$	6037 ± 77 (1)	-0.04 ± 0.1 (1)	$4.295^{+0.009}_{-0.009}$	$\cdots$
6116048	$\cdots$	8.42	Q5.1–Q17.2	$2126.9^{+5.5}_{-5.0}$	$100.754^{+0.017}_{-0.017}$	6033 ± 77 (1)	-0.23 ± 0.1 (1)	$4.254^{+0.012}_{-0.009}$	17.26 ± 1.96 (9)
6225718	$\cdots$	7.5	Q6.1–Q17.2	$2364.2^{+4.9}_{-4.6}$	$105.695^{+0.018}_{-0.017}$	6313 ± 77 (1)	-0.07 ± 0.1 (1)	$4.319^{+0.007}_{-0.005}$	$\cdots$
6278762	3158	8.73	Q15.1–Q17.2	$4538.0^{+144.0}_{-144.0}$	$179.640^{+0.760}_{-0.760}$	5046 ± 74 (2)	-0.37 ± 0.09 (2)	$4.560^{+0.003}_{-0.002}$	$\cdots$
6508366	$\cdots$	8.97	Q5.1–Q17.2	$958.3^{+4.6}_{-3.6}$	$51.553^{+0.046}_{-0.047}$	6331 ± 77 (1)	-0.05 ± 0.1 (1)	$3.942^{+0.007}_{-0.005}$	3.7 ± 0.35 (9)
6521045	41	11.2	Q3.1–Q17.2	$1502.0^{+31.0}_{-31.0}$	$77.000^{+1.100}_{-1.100}$	5825 ± 75 (2)	0.02 ± 0.1 (2)	$4.125^{+0.004}_{-0.004}$	24.988 ± 2.192 (10)
6603624	$\cdots$	9.09	Q5.1–Q17.2	$2384.0^{+5.4}_{-5.6}$	$110.128^{+0.012}_{-0.012}$	5674 ± 77 (1)	0.28 ± 0.1 (1)	$4.320^{+0.005}_{-0.004}$	$\cdots$
6679371	$\cdots$	8.73	Q5.1–Q17.2	$941.8^{+5.1}_{-5.0}$	$50.601^{+0.029}_{-0.029}$	6479 ± 77 (1)	0.01 ± 0.1 (1)	$3.934^{+0.008}_{-0.007}$	5.48 ± 0.5 (9)
6933899	$\cdots$	9.62	Q5.1–Q17.2	$1389.9^{+3.9}_{-3.6}$	$72.135^{+0.018}_{-0.018}$	5832 ± 77 (1)	-0.01 ± 0.1 (1)	$4.079^{+0.009}_{-0.008}$	$\cdots$
7103006	$\cdots$	8.86	Q5.1–Q17.2	$1167.9^{+7.2}_{-6.9}$	$59.658^{+0.029}_{-0.030}$	6344 ± 77 (1)	0.02 ± 0.1 (1)	$4.015^{+0.007}_{-0.007}$	4.733 ± 0.059 (12)
7106245	$\cdots$	10.79	Q5.1–Q15.3	$2397.9^{+24.0}_{-28.7}$	$111.376^{+0.063}_{-0.061}$	6068 ± 102 (3)	-0.99 ± 0.19 (3)	$4.310^{+0.008}_{-0.010}$	$\cdots$
7206837	$\cdots$	9.77	Q5.1– Q17.2	$1652.5^{+10.6}_{-11.0}$	$79.130^{+0.037}_{-0.039}$	6305 ± 77 (1)	0.1 ± 0.1 (1)	$4.163^{+0.007}_{-0.008}$	4.072 ± 0.005 (12)
7296438	364	10.09	Q7.1–Q11.3	$1847.8^{+8.5}_{-12.6}$	$88.698^{+0.040}_{-0.036}$	5775 ± 77 (1)	0.19 ± 0.1 (1)	$4.201^{+0.010}_{-0.009}$	25.16 ± 2.78 (9)
7510397	$\cdots$	7.77	Q7.1–Q17.2	$1189.1^{+3.4}_{-4.4}$	$62.249^{+0.020}_{-0.020}$	6171 ± 77 (1)	-0.21 ± 0.1 (1)	$4.036^{+0.004}_{-0.007}$	$\cdots$
7670943	269	10.93	Q6.1–Q17.2	$1895.0^{+73.0}_{-73.0}$	$88.600^{+1.300}_{-1.300}$	6463 ± 110 (2)	0.09 ± 0.11 (2)	$4.228^{+0.008}_{-0.008}$	5.274 ± 0.033 (10)
7680114	$\cdots$	10.07	Q5.1–Q17.2	$1709.1^{+7.1}_{-6.5}$	$85.145^{+0.039}_{-0.043}$	5811 ± 77 (1)	0.05 ± 0.1 (1)	$4.172^{+0.010}_{-0.008}$	26.31 ± 1.86 (9)
7771282	$\cdots$	10.77	Q5.1–Q11.3	$1465.1^{+27.0}_{-18.7}$	$72.463^{+0.069}_{-0.079}$	6248 ± 77 (1)	-0.02 ± 0.1 (1)	$4.112^{+0.007}_{-0.007}$	11.744 ± 0.23 (12)
7871531	$\cdots$	9.25	Q5.1–Q17.2	$3455.9^{+19.3}_{-26.5}$	$151.329^{+0.025}_{-0.023}$	5501 ± 77 (1)	-0.26 ± 0.1 (1)	$4.478^{+0.005}_{-0.007}$	35.361 ± 0.218 (12)
7940546	$\cdots$	7.4	Q7.1–Q17.2	$1116.6^{+3.3}_{-3.6}$	$58.762^{+0.029}_{-0.029}$	6235 ± 77 (1)	-0.2 ± 0.1 (1)	$4.000^{+0.002}_{-0.002}$	11.36 ± 0.95 (9)
7970740	$\cdots$	7.78	Q6.1–Q17.2	$4197.4^{+21.2}_{-18.4}$	$173.541^{+0.060}_{-0.068}$	5309 ± 77 (1)	-0.54 ± 0.1 (1)	$4.539^{+0.005}_{-0.004}$	17.97 ± 3.09 (9)
8006161	$\cdots$	7.36	Q5.1–Q17.2	$3574.7^{+11.4}_{-10.5}$	$149.427^{+0.015}_{-0.014}$	5488 ± 77 (1)	0.34 ± 0.1 (1)	$4.494^{+0.007}_{-0.007}$	29.79 ± 3.09 (9)
8077137	274	11.39	Q6.1–Q17.2	$1324.0^{+39.0}_{-39.0}$	$68.800^{+0.640}_{-0.640}$	6072 ± 75 (2)	-0.09 ± 0.1 (2)	$4.056^{+0.013}_{-0.010}$	$\cdots$
8150065	$\cdots$	10.74	Q5.1–Q10.3	$1876.9^{+38.1}_{-32.4}$	$89.264^{+0.134}_{-0.121}$	6173 ± 101 (3)	-0.13 ± 0.15 (3)	$4.220^{+0.008}_{-0.008}$	$\cdots$
8179536	$\cdots$	9.46	Q5.1–Q11.3	$2074.9^{+13.8}_{-12.0}$	$95.090^{+0.058}_{-0.054}$	6343 ± 77 (1)	-0.03 ± 0.1 (1)	$4.255^{+0.010}_{-0.010}$	24.55 ± 1.61 (9)
8228742	$\cdots$	9.37	Q5.1–Q17.2	$1190.5^{+3.4}_{-3.7}$	$62.071^{+0.022}_{-0.021}$	6122 ± 77 (1)	-0.08 ± 0.1 (1)	$4.032^{+0.004}_{-0.005}$	20.23 ± 2.16 (9)
8292840	260	10.5	Q5.1–Q17.2	$1983.0^{+35.0}_{-35.0}$	$92.850^{+0.350}_{-0.350}$	6239 ± 94 (2)	-0.14 ± 0.1 (2)	$4.240^{+0.008}_{-0.008}$	$\cdots$
8379927	$\cdots$	6.96	Q2.1–Q17.2	$2795.3^{+6.0}_{-5.7}$	$120.288^{+0.017}_{-0.018}$	6067 ± 120 (5)	-0.1 ± 0.15 (5)	$4.388^{+0.007}_{-0.008}$	17.259 ± 0.026 (12)
8394589	$\cdots$	9.52	Q5.1–Q17.2	$2396.7^{+10.5}_{-9.4}$	$109.488^{+0.034}_{-0.035}$	6143 ± 77 (1)	-0.29 ± 0.1 (1)	$4.322^{+0.008}_{-0.008}$	$\cdots$
8424992	$\cdots$	10.32	Q7.1–Q10.3	$2533.7^{+27.0}_{-28.1}$	$120.584^{+0.062}_{-0.062}$	5719 ± 77 (1)	-0.12 ± 0.1 (1)	$4.359^{+0.007}_{-0.007}$	$\cdots$
8478994	245	9.71	Q5.1–Q17.2	$4660.0^{+50.0}_{-50.0}$	$178.700^{+1.400}_{-1.400}$	5417 ± 75 (2)	-0.32 ± 0.07 (2)	$4.570^{+0.003}_{-0.002}$	28.79 ± 3.29 (13)
8494142	370	11.93	Q7.1–Q17.2	$1133.0^{+81.0}_{-81.0}$	$61.800^{+0.760}_{-0.760}$	6144 ± 106 (2)	0.13 ± 0.1 (2)	$4.038^{+0.005}_{-0.005}$	$\cdots$
8694723	$\cdots$	8.88	Q5.1–Q17.2	$1470.5^{+3.7}_{-4.1}$	$75.112^{+0.019}_{-0.021}$	6246 ± 77 (1)	-0.42 ± 0.1 (1)	$4.113^{+0.009}_{-0.007}$	7.5 ± 0.2 (14)
8760414	$\cdots$	9.62	Q5.1–Q17.2	$2455.3^{+9.1}_{-8.3}$	$117.230^{+0.022}_{-0.018}$	5873 ± 77 (1)	-0.92 ± 0.1 (1)	$4.320^{+0.003}_{-0.007}$	$\cdots$
8866102	42	9.36	Q3.1–Q17.2	$2014.0^{+32.0}_{-32.0}$	$94.500^{+0.270}_{-0.270}$	6325 ± 75 (2)	0.01 ± 0.1 (2)	$4.262^{+0.007}_{-0.007}$	20.85 ± 0.007 (10)
8938364	$\cdots$	10.11	Q6.1–Q17.2	$1675.1^{+5.2}_{-5.8}$	$85.684^{+0.018}_{-0.020}$	5677 ± 77 (1)	-0.13 ± 0.1 (1)	$4.173^{+0.002}_{-0.007}$	$\cdots$
9025370	$\cdots$	8.85	Q5.1–Q17.2	$2988.6^{+20.0}_{-16.9}$	$132.628^{+0.030}_{-0.024}$	5270 ± 180 (6)	-0.12 ± 0.18 (6)	$4.423^{+0.004}_{-0.007}$	13.31 ± 1.30 (9)
9098294	$\cdots$	9.76	Q5.1–Q17.2	$2314.7^{+9.2}_{-10.4}$	$108.894^{+0.023}_{-0.022}$	5852 ± 77 (1)	-0.18 ± 0.1 (1)	$4.308^{+0.007}_{-0.005}$	20.119 ± 0.144 (12)
9139151	$\cdots$	9.18	Q5.1–Q17.2	$2690.4^{+14.5}_{-9.0}$	$117.294^{+0.031}_{-0.032}$	6302 ± 77 (1)	0.1 ± 0.1 (1)	$4.382^{+0.008}_{-0.008}$	10.96 ± 2.22 (11)
9139163	$\cdots$	8.33	Q5.1–Q17.2	$1729.8^{+6.2}_{-5.9}$	$81.170^{+0.042}_{-0.036}$	6400 ± 84 (3)	0.15 ± 0.09 (3)	$4.200^{+0.008}_{-0.009}$	6.1 ± 0.47 (9)
9206432	$\cdots$	9.08	Q5.1–Q12.3	$1866.4^{+10.3}_{-14.9}$	$84.926^{+0.046}_{-0.051}$	6538 ± 77 (1)	0.16 ± 0.1 (1)	$4.220^{+0.007}_{-0.005}$	8.8 ± 1.06 (9)

Table 1
(Continued)

KIC	KOI	Kp	Quarters	ν_{max} (μHz)	$\Delta\nu$ (μHz)	T_{eff} (K)	[Fe/H] (dex)	log g (dex)	P_{rot} (days)
9353712	⋯	10.84	Q5.1–Q12.3	$934.3^{+11.1}_{-8.3}$	$51.467^{+0.091}_{-0.104}$	6278 ± 77 (1)	-0.05 ± 0.1 (1)	$3.943^{+0.005}_{-0.007}$	11.3 ± 1.12 (9)
9410862	⋯	10.71	Q5.1–Q15.3	$2278.8^{+31.2}_{-16.6}$	$107.390^{+0.050}_{-0.053}$	6047 ± 77 (1)	-0.31 ± 0.1 (1)	$4.300^{+0.008}_{-0.009}$	22.77 ± 2.37 (9)
9414417	974	9.58	Q6.1–Q17.2	$1155.3^{+6.1}_{-4.6}$	$60.115^{+0.024}_{-0.024}$	6253 ± 75 (7)	-0.13 ± 0.1 (7)	$4.016^{+0.005}_{-0.005}$	10.847 ± 0.002 (10)
9592705	288	11.02	Q6.1–Q17.2	$1008.0^{+21.0}_{-21.0}$	$53.540^{+0.320}_{-0.320}$	6174 ± 92 (2)	0.22 ± 0.1 (2)	$3.961^{+0.004}_{-0.003}$	13.38 ± 0.095 (10)
9812850	⋯	9.47	Q5.1–Q17.2	$1255.2^{+9.1}_{-7.0}$	$64.746^{+0.067}_{-0.068}$	6321 ± 77 (1)	-0.07 ± 0.1 (1)	$4.053^{+0.009}_{-0.008}$	5.19 ± 0.79 (9)
9955598	1295	9.44	Q5.1–Q17.2	$3616.8^{+21.2}_{-29.6}$	$153.283^{+0.029}_{-0.032}$	5457 ± 77 (1)	0.05 ± 0.1 (1)	$4.497^{+0.005}_{-0.005}$	34.2 ± 5.64 (9)
9965715	⋯	9.34	Q5.1–Q13.3	$2079.3^{+9.2}_{-10.4}$	$97.236^{+0.041}_{-0.040}$	5860 ± 180 (6)	-0.44 ± 0.18 (6)	$4.272^{+0.009}_{-0.007}$	⋯
10068307	⋯	8.18	Q7.1–Q17.2	$995.1^{+2.8}_{-2.7}$	$53.945^{+0.019}_{-0.020}$	6132 ± 77 (1)	-0.23 ± 0.1 (1)	$3.967^{+0.004}_{-0.004}$	18.6 ± 2.07 (9)
10079226	⋯	10.07	Q7.1–Q10.3	$2653.0^{+47.7}_{-44.3}$	$116.345^{+0.059}_{-0.052}$	5949 ± 77 (1)	0.11 ± 0.1 (1)	$4.366^{+0.005}_{-0.005}$	15.694 ± 0.165 (12)
10162436	⋯	8.61	Q5.1–Q17.2	$1052.0^{+4.0}_{-4.2}$	$55.725^{+0.035}_{-0.039}$	6146 ± 77 (1)	-0.16 ± 0.1 (1)	$3.981^{+0.005}_{-0.005}$	12.331 ± 0.327 (12)
10454113	⋯	8.62	Q5.1–Q17.2	$2357.2^{+8.2}_{-9.1}$	$105.063^{+0.031}_{-0.033}$	6177 ± 77 (1)	-0.07 ± 0.1 (1)	$4.314^{+0.005}_{-0.005}$	14.448 ± 0.229 (12)
10516096	⋯	9.46	Q5.1–Q17.2	$1689.8^{+4.6}_{-5.8}$	$84.424^{+0.022}_{-0.025}$	5964 ± 77 (1)	-0.11 ± 0.1 (1)	$4.169^{+0.011}_{-0.010}$	⋯
10586004	275	11.7	Q6.1–Q7.3	$1395.0^{+40.0}_{-40.0}$	$69.200^{+1.400}_{-1.400}$	5770 ± 83 (2)	0.29 ± 0.1 (2)	$4.071^{+0.005}_{-0.005}$	29.79 ± 1.02 (11)
10644253	⋯	9.16	Q5.1–Q17.2	$2899.7^{+21.3}_{-22.8}$	$123.080^{+0.056}_{-0.055}$	6045 ± 77 (1)	0.06 ± 0.1 (1)	$4.396^{+0.008}_{-0.007}$	10.91 ± 0.87 (9)
10666592	2	10.46	Q0.0–Q17.2	$1115.0^{+110.0}_{-110.0}$	$59.220^{+0.590}_{-0.590}$	6350 ± 80 (2)	0.26 ± 0.08 (2)	$4.017^{+0.007}_{-0.009}$	⋯
10730618	⋯	10.45	Q0.0–Q11.3	$1282.1^{+14.6}_{-12.7}$	$66.333^{+0.061}_{-0.064}$	6150 ± 180 (6)	-0.11 ± 0.18 (6)	$4.062^{+0.007}_{-0.008}$	⋯
10963065	1612	8.77	Q2.3–Q17.2	$2203.7^{+6.7}_{-6.3}$	$103.179^{+0.027}_{-0.027}$	6140 ± 77 (1)	-0.19 ± 0.1 (1)	$4.277^{+0.011}_{-0.011}$	12.444 ± 0.172 (10)
11081729	⋯	9.03	Q5.1–Q17.2	$1968.3^{+11.0}_{-12.6}$	$90.116^{+0.048}_{-0.047}$	6548 ± 83 (1)	0.11 ± 0.1 (1)	$4.245^{+0.009}_{-0.010}$	2.74 ± 0.31 (9)
11253226	⋯	8.44	Q5.1–Q17.2	$1590.6^{+10.6}_{-6.8}$	$76.858^{+0.026}_{-0.030}$	6642 ± 77 (1)	-0.08 ± 0.1 (1)	$4.173^{+0.004}_{-0.005}$	3.64 ± 0.37 (9)
11295426	246	10.0	Q2.3–Q17.2	$2154.0^{+13.0}_{-13.0}$	$101.570^{+0.100}_{-0.100}$	5793 ± 74 (2)	0.12 ± 0.07 (2)	$4.280^{+0.003}_{-0.003}$	⋯
11401755	277	11.87	Q6.1–Q17.2	$1250.0^{+44.0}_{-44.0}$	$67.900^{+1.200}_{-1.200}$	5911 ± 66 (2)	-0.2 ± 0.06 (2)	$4.039^{+0.004}_{-0.004}$	17.04 ± 0.98 (11)
11772920	⋯	9.66	Q5.1–Q17.2	$3674.7^{+55.1}_{-36.1}$	$157.746^{+0.032}_{-0.033}$	5180 ± 180 (6)	-0.09 ± 0.18 (6)	$4.500^{+0.008}_{-0.005}$	⋯
11807274	262	10.42	Q6.1–Q17.2	$1496.0^{+56.0}_{-56.0}$	$75.710^{+0.310}_{-0.310}$	6225 ± 75 (2)	0.0 ± 0.08 (2)	$4.135^{+0.007}_{-0.009}$	7.553 ± 0.755 (10)
11904151	72	10.96	Q2.2–Q17.2	$2730.0^{+280.0}_{-280.0}$	$118.200^{+0.200}_{-0.200}$	5647 ± 74 (2)	-0.15 ± 0.1 (2)	$4.344^{+0.003}_{-0.003}$	21.9 ± 3.0 (15)
12009504	⋯	9.32	Q5.1–Q17.2	$1865.6^{+7.7}_{-6.2}$	$88.217^{+0.026}_{-0.025}$	6179 ± 77 (1)	-0.08 ± 0.1 (1)	$4.211^{+0.005}_{-0.007}$	9.426 ± 0.327 (12)
12069127	⋯	10.7	Q5.1–Q11.3	$884.7^{+10.1}_{-8.0}$	$48.400^{+0.048}_{-0.048}$	6276 ± 77 (1)	0.08 ± 0.1 (1)	$3.912^{+0.004}_{-0.005}$	0.92 ± 0.05 (9)
12069424	⋯	5.86	Q6.1–Q17.2	$2188.5^{+4.6}_{-3.0}$	$103.277^{+0.021}_{-0.020}$	5825 ± 50 (8)	0.1 ± 0.03 (8)	$4.287^{+0.007}_{-0.007}$	23.80 ± 1.80 (16)
12069449	⋯	6.09	Q6.1–Q17.2	$2561.3^{+5.0}_{-5.6}$	$116.929^{+0.012}_{-0.013}$	5750 ± 50 (8)	0.05 ± 0.02 (8)	$4.353^{+0.005}_{-0.007}$	23.20 ± 6.00 (16)
12258514	⋯	8.08	Q5.1–Q17.2	$1512.7^{+3.3}_{-2.9}$	$74.799^{+0.016}_{-0.015}$	5964 ± 77 (1)	-0.0 ± 0.1 (1)	$4.126^{+0.003}_{-0.004}$	15.0 ± 1.84 (9)
12317678	⋯	8.74	Q5.1–Q17.2	$1212.4^{+5.5}_{-4.9}$	$63.464^{+0.025}_{-0.024}$	6580 ± 77 (1)	-0.28 ± 0.1 (1)	$4.048^{+0.009}_{-0.008}$	⋯

Note. References: frequency of the maximum power (ν_{max}) and large frequency separation ($\Delta\nu$) are from Davies et al. (2016) or Lund et al. (2017). Effective temperature (T_{eff}) and metallicity ([Fe/H]) are from (1) Lund et al. (2017); (2) Silva Aguirre et al. (2015); (3) Chaplin et al. (2014); (4) Casagrande et al. (2014); (5) Pinsonneault et al. (2012); (6) Pinsonneault et al. (2014); (7) Huber et al. (2013); or (8) Ramírez et al. (2009). Surface gravity (log g) is from Silva Aguirre et al. (2015, 2017). Rotation period (P_{rot}) is from (9) García et al. (2014); (10) McQuillan et al. (2014); (11) Ceillier et al. (2016); (12) McQuillan et al. (2013); (13) Walkowicz & Basri (2013); (14) Karoff et al. (2013b); (15) Dumusque et al. (2014); or (16) Davies et al. (2015). Each quarter corresponds to one-quarter of *Kepler*'s year (∼372.5 days).

indicators of a solar-type star (HD 49933) observed by the *CoRoT* (*Convection, Rotation, and planetary Transits*; Baglin et al. 2006) space telescope. Similarly to what is observed in the Sun, the mode amplitudes and frequency shifts are anti-correlated in time and show a temporal offset in relation to the photometric indicator. The second detection of activity-related frequency shifts in a star other than the Sun was reported by Salabert et al. (2016b). The authors found temporal frequency shifts varying consistently with the photometric activity indicator, S_{ph} (García et al. 2014; Mathur et al. 2014), in the active solar-type star KIC 10644253, observed by the *Kepler* main mission (Borucki et al. 2010). They also mentioned the possibility that the frequency shift they found could be related to a short-term modulation, similar to the quasi-biennial modulation in the Sun. In spite of the large uncertainties, Régulo et al. (2016) found evidence for frequency shifts in the active solar-type star KIC 3733735, which seem to be ahead in time relative to the S_{ph}. Kiefer et al. (2017) analyzed 24 solar-type stars

observed by *Kepler*, searching for variations in the mode frequencies through a cross-correlation method and in the height of the p-mode envelope. The authors reported significant frequency shifts in 23 stars and evidence for activity-related frequency shifts in six of them. Salabert et al. (2018) studied the frequency dependence of the frequency shifts observed in *Kepler* solar-type stars. The results for the four best stars in their sample suggest that the main source for the observed frequency shifts in the Sun and in those stars may be different.

In this work, we analyze the short-cadence data of 87 solar-type stars observed by the *Kepler* main mission. The main goal is to search for temporal variations of the acoustic frequencies, that may be related to stellar activity. To that end, we developed a Bayesian peak-bagging tool to estimate the mode parameters. For each star, we present and provide the temporal mean frequency shifts (including those for the individual angular degrees), the temporal evolution of the mode heights, and the characteristic timescale of the granulation.
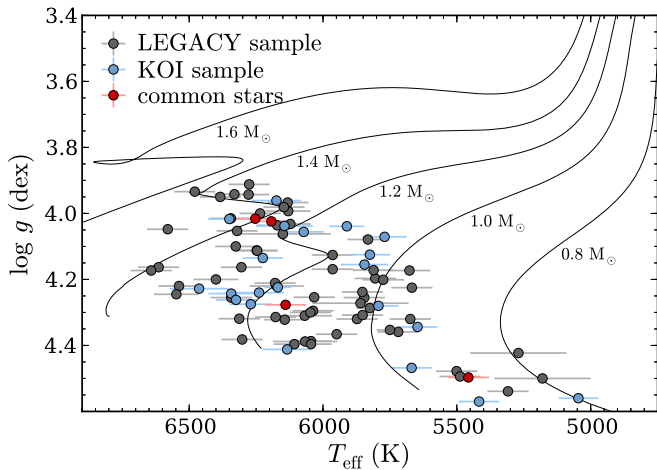
Figure 1. Kiel-diagram for the stars in the target sample, which is composed of the LEGACY sample (gray dots) and a sample of 25 KOIs (blue dots). The red dots mark the stars that are common to both sub-samples. The black solid lines show the solar-calibrated evolutionary tracks obtained with the evolution code Modules for Experiments in Stellar Astrophysics (MESA; Paxton et al. 2011, 2013).

2. Methodology

2.1. Target Sample

The main goal of this work is to search for temporal frequency shifts, possibly related to magnetic activity, in a large sample of *Kepler* targets. In order to successfully detect and characterize solar-type oscillations, we analyze the short-cadence ($\Delta t = 58.85$ s) data of 87 *Kepler* solar-type stars, selected from two samples previously studied in the literature (with four common stars). Most of these stars (66) are high signal-to-noise ratio solar-type pulsators that constitute the LEGACY sample (Lund et al. 2017; Silva Aguirre et al. 2017). The other group of targets is composed of 25 solar-type *Kepler* Objects of Interest (KOIs) that were analyzed by Campante et al. (2016) in the context of the spin–orbit alignment of the exoplanet systems. These KOIs were also part of a larger sample analyzed by Silva Aguirre et al. (2015) and Davies et al. (2016). The stellar parameters of the 87 *Kepler* solar-type stars are summarized in Table 1 and Figure 1 displays the target sample in a Kiel-diagram (i.e., $\log g$ versus $T_{\rm eff}$).

2.2. Data Preparation

The pixel data of the sample stars were collected from the *Kepler* Asteroseismic Science Operations Center (KASOC; http://kasoc.phys.au.dk) and then corrected using the KASOC filter (Handberg & Lund 2014). For further details see Lund et al. (2017, Section 2.1).

To search for temporal variations of the acoustic frequencies of the *Kepler* targets, the original time-series were divided into sub-series of 90 days overlapped by 45 days. The respective power-density spectra are obtained as the periodogram of each sub-series, normalized so that Parseval's theorem is satisfied.

For the photometric magnetic activity proxy, $S_{\rm ph}$ (see Section 2.3), we use KADACS (*Kepler* Asteroseismic Data Analysis and Calibration Software) light curves obtained from the long-cadence data, corrected following the approach described in García et al. (2011) and high-pass filtered at

20 and 55 days, allowing rotation periods measurements as long as 90 days.

2.3. Photometric Magnetic Activity Proxy

García et al. (2010) showed, in the case of the *CoRoT* solar-type star HD 49933, that the fluctuations associated with the presence of spots or magnetic features rotating on the surface of the star can provide a global proxy of stellar magnetic activity. However, brightness variability can have different origins with various timescales, such as convective motions, oscillations, stellar companion, or instrumental problems. Therefore, to compute such a magnetic activity proxy, the stellar rotation period, $P_{\rm rot}$, needs to be taken into account. The so-called photometric activity proxy, $S_{\rm ph}$, is estimated as the standard deviations calculated over sub-series of length $5 \times P_{\rm rot}$. Mathur et al. (2014) demonstrated that $S_{\rm ph}$ provides a global proxy only related to magnetism and not to other sources of variability. Furthermore, both long-term (11 years) and short-term (quasi-biennial) variations can be monitored through the $S_{\rm ph}$, as shown in the case of the Sun (Salabert et al. 2017). Also, Salabert et al. (2016a) showed the complementarity between $S_{\rm ph}$ and the chromospheric activity measured as the Ca K-line emission index (Wilson 1978). Unlike chromospheric activity proxies, $S_{\rm ph}$ can be easily estimated from space photometric observations for a large number of stars with known rotation period. Chromospheric activity proxies require a large amount of ground-based telescope time to collect enough spectroscopic data for each individual target, and this is only possible for bright targets.

2.4. Background Signal

The power spectrum of solar-type stars may enclose the signature of different stellar phenomena, such as active regions, granulation, faculae, and acoustic oscillations. We describe the granular and facular components through a Harvey-like profile (e.g., Harvey 1985; García et al. 2009; Campante et al. 2011; Handberg & Campante 2011; Mathur et al. 2011; Karoff 2012; Davies et al. 2016)

$$f(\nu) = \frac{H}{1 + (2\pi\nu\tau)^{\alpha}}, \tag{1}$$

where $H = 4\sigma^2\tau$ is the amplitude of the granulation power, σ and τ are, respectively, the characteristic amplitude and timescale, and α is the slope of the power law. For the activity component, we use a power law of the form

$$f(\nu) = \frac{H_{\rm act}}{\nu^2}, \tag{2}$$

which results from considering a Harvey-like profile (Equation (1)) in the limit $2\pi\tau_{\rm act} \gg 1$ with $\alpha = 2$, found to be adequate in describing the exponential decay of active regions (e.g., García et al. 2009; Campante et al. 2016). Finally, to properly model the background signal, one needs to consider a flat component, N, related to the photon shot-noise.

We start by considering two competing background models. The first model considers three components ($p = 5$ parameters): activity, granulation, and photon shot-noise. The second background model further includes a facular component ($p + n = 8$ parameters). To test the statistical significance of
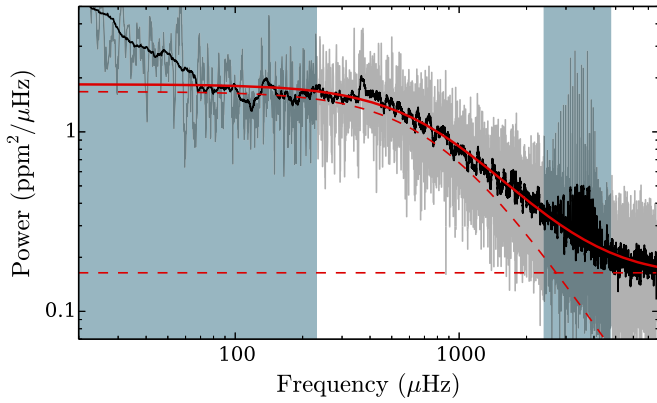
Figure 2. Power-density spectrum (gray and black; with different smoothing for illustrative purposes) of a 90-day sub-series for the solar-type star KIC 8006161. The red solid line shows the best background model and the dashed lines show the different background components. The blue areas mark the frequency intervals neglected from the fitting process.

Figure 3. Granulation timescale as a function of $\nu_{\max}$ for the stars in the sample. The blue and red lines show the best fits ($\tau_{\mathrm{gran}} = A\nu_{\max}^B$ and $\tau_{\mathrm{gran}} = A\nu_{\max}^B + C$, respectively). For comparison, the yellow star marks the position of the Sun with $\nu_{\max,\odot} = 3090\,\mu$Hz (e.g., Huber et al. 2011) and $\tau_{\mathrm{gran},\odot}$ computed in Appendix A.1.

the additional model parameters, we compute the respective likelihood ratio, Λ (e.g., Appourchaux et al. 1998; Karoff 2012; Karoff et al. 2013a). When $\Lambda \ll 1$, we can conclude that the n additional parameters are not needed to describe the background signal from a statistical viewpoint.

For a large number of sub-series, we find that the facular component is not significant enough. Therefore, in order to be consistent in the analysis, the final background model, which we apply to all *Kepler* targets, corresponds to the first of the tested models, i.e.,

$$\mathcal{B}(\nu) = \left[\frac{H_{\mathrm{act}}}{\nu^2} + \frac{H_{\mathrm{gran}}}{1 + (2\pi\nu\tau_{\mathrm{gran}})^{\alpha_{\mathrm{gran}}}} \right] \eta^2(\nu) + N, \qquad (3)$$

where

$$\eta = \mathrm{sinc}\left(\frac{\pi}{2} \frac{\nu}{\nu_{\mathrm{Nyquist}}} \right) \qquad (4)$$

describes the apodization resulting from the sampling of the signal (Chaplin et al. 2011), and ν_{Nyquist} is the Nyquist frequency.

In this step of the analysis, we exclude the low-frequency range (with frequency cutoff defined as $200 \times \nu_{\max}/\nu_{\max,\odot}\,\mu$Hz), which is dominated by an activity component. Still, we model the activity component in order to prevent any contamination (due to spectral leakage) into the frequency range where the granulation component becomes important. While fitting the background, we also exclude the frequency range of the p-modes (centered at $\nu_{\max}$ and with a width of $2/3\,\nu_{\max}$).

The model parameters that best describe the background signal are obtained through maximum likelihood estimation (MLE) and the formal errors are derived from the inverse Hessian matrix (e.g., Toutain & Appourchaux 1994; Campante et al. 2011). The background parameters are then fixed for each sub-series in the subsequent peak-bagging analysis (Section 2.5). As an example, Figure 2 shows the power-density spectrum of a 90-day sub-series for one of the stars in the sample, namely KIC 8006161.

As the convection is the mechanism behind both granulation and acoustic oscillations, the granulation characteristic timescale, τ_{gran}, is expected to be related to the timescale of the p-modes, and thus to $\nu_{\max}$. Huber et al. (2009) suggested that τ_{gran} scales inversely to $\nu_{\max}$, i.e., $\tau_{\mathrm{gran}} \propto 1/\nu_{\max}$ (see also Kjeldsen & Bedding 2011). This means that larger stars are expected to have longer granulation timescales than smaller stars. Kallinger & Matthews (2010, based on *CoRoT* red giant and main-sequence solar-type pulsators), Mathur et al. (2011, based on *Kepler* red giants), and Kallinger et al. (2014, based on *Kepler* main-sequence stars, sub-giants, and red giants) confirmed the empirical prediction by Huber et al. (2009), finding that the granulation timescale is approximately proportional to $\nu_{\max}^{-1}$.

Figure 3 shows the granulation timescale for the stars in the sample, computed as the weighted average over the independent sub-series (i.e., every second sub-series), as a function of $\nu_{\max}$. The yellow star marks the position of the Sun, and the red and blue lines mark the best fits to the data. The fit shown in blue is obtained when fitting a function of the form $\tau_{\mathrm{gran}} = A\nu_{\max}^B$ (fit 1), where $A = (1.7 \pm 0.3) \times 10^4$ and $B = -0.55 \pm 0.02$. If we consider an extra parameter, a constant C, i.e., $\tau_{\mathrm{gran}} = A\nu_{\max}^B + C$ (fit 2), we will find the best fit shown in red with $A = (2.1 \pm 2.7) \times 10^5$, $B = -1.0 \pm 0.2$, and $C = 110 \pm 40$. The value found for the exponent B differs from that found in previous studies, where $B = -0.89$ (Mathur et al. 2011; Kallinger et al. 2014). This difference may arise from the type of stars used in the different studies. The results presented here are based on a sample of solar-type stars with $\nu_{\max}$ between 880 and 4660 μHz.

2.5. Bayesian Peak-bagging Tool

In order to perform the global (simultaneous) fit of the acoustic modes, we follow a Bayesian approach (e.g., Benomar et al. 2009; Campante et al. 2011; Handberg & Campante 2011; Davies et al. 2016; Lund et al. 2017), through the implementation of the Affine Invariant Markov Chain Monte Carlo (MCMC) Ensemble sampler emcee (Goodman & Weare 2010; Foreman-Mackey et al. 2013). In the Bayesian framework, the posterior probability for a set of model parameters, Θ, given the observational data D and the available prior information I,

i.e., $p(\boldsymbol{\Theta}|D, I)$, is obtained through Bayes' theorem

$$p(\boldsymbol{\Theta}|D, I) = \frac{p(\boldsymbol{\Theta}|I)p(D|\boldsymbol{\Theta}, I)}{p(D|I)}, \qquad (5)$$

where $p(\boldsymbol{\Theta}|I)$ is the prior probability of the parameters, $p(D|\boldsymbol{\Theta}, I)$ is the likelihood function, and $p(D|I)$ is a normalization factor.

The power-density spectrum of a solar-type star contains a number of oscillation modes characterized by the wave numbers n, l, and m (radial order, angular degree, and azimuthal order, respectively). To model the power-density spectrum of each oscillation mode, we use a standard Lorentzian profile. The final model of the acoustic spectrum is then given by

$$\mathcal{M}(\nu) = \sum_{n=n_0}^{n_1} \sum_{l=0}^{l_1} \sum_{m=-l}^{l} \frac{H_{nlm}}{1 + \frac{4}{\Gamma_{nlm}^2}(\nu - \nu_{nl} - m\nu_s)^2}, \qquad (6)$$

where n_0 and n_1 are the first and last radial orders considered in the global fit, l_1 is the highest angular degree visible within a radial order n, ν_{nl} and Γ_{nlm} are the mode frequency and line width, and ν_s represents the rotational splitting. The mode height H_{nlm} is given by

$$H_{nlm} = \mathcal{E}_{lm}(i)\,\widetilde{V}_l^2\,S_{nl}, \qquad (7)$$

where $\mathcal{E}_{lm}$ represents the relative mode visibility within the (n, l) multiplet (Gizon & Solanki 2003), i is the stellar inclination angle, $\widetilde{V}_l = V_l/V_{l=0}$ and V_l is related to the geometrical visibility of the multiplet, and S_{nl} is the multiplet's overall height. The geometrical visibilities for *Kepler* targets are taken from Handberg & Campante (2011).

The final model of the stellar power spectrum corresponds to

$$\mathcal{P}(\nu; \boldsymbol{\Theta}) = \mathcal{M}(\nu) + \mathcal{B}(\nu). \qquad (8)$$

In our analysis, only the line widths and heights of the radial modes, Γ_{n0} and S_{n0}, are considered free parameters. For the quadrupole modes, we consider the line width and height of the closest radial mode, since their frequencies do not differ by much. For the dipolar modes, we linearly interpolate between the two closest radial orders. Thus, the final set of free parameters is

$$\boldsymbol{\Theta} = \{\nu_{nl}, S_{n0}, \Gamma_{n0}, \nu_s, i\}. \qquad (9)$$

Assuming a χ^2 with two degrees of freedom statistics for the power spectrum (Duvall & Harvey 1986; Anderson et al. 1990; Gabriel 1994), the logarithm of the likelihood function is given by

$$\mathcal{L}(\boldsymbol{\Theta}) \equiv \ln L(\boldsymbol{\Theta}) = -\sum_j \left\{ \ln \mathcal{P}(\nu_j; \boldsymbol{\Theta}) + \frac{P_j}{\mathcal{P}(\nu_j; \boldsymbol{\Theta})} \right\}, \quad (10)$$

where $\mathcal{P}(\nu_j; \boldsymbol{\Theta})$ corresponds to the mean power spectrum, which we model (Equation (8)), and P_j is the observed power. We use logarithmic probabilities to ensure numerical stability.

One of the main strengths of a Bayesian approach is the possibility of using prior knowledge in the analysis. In what follows, we summarize the prior functions that we assume for the model parameters (mode frequencies, heights, and line widths of the radial modes, rotational splitting, and stellar inclination angle) and the fitting method.

2.5.1. Prior Probabilities

Mode frequencies. For the mode frequencies we use uniform priors, whose lower and upper limits are defined as $\nu_{nl}^0 \pm 4\ \mu$Hz, where the values ν_{nl}^0 are taken from the literature, namely from Davies et al. (2016) and Lund et al. (2017). We further constrain the mode frequencies using priors on the large and small frequency separations ($\Delta\nu$ and $d\nu$, respectively), which are expected to vary smoothly from one order to the next. Following the approach of Davies et al. (2016), we define the prior functions for the large and small frequency separations as

$$\ln f(\Delta\nu_l) = -0.125 \sum_{n=n_0}^{n_{\max}} \left(\frac{\partial^2 \nu_{nl}}{\partial n^2}\right)^2, \qquad (11)$$

$$\ln f(d\nu_{l,l+2}) = -0.25 \sum_{n=n_0}^{n_{\max}} \left(\frac{\partial d\nu_{l,l+2}}{\partial n}\right)^2. \qquad (12)$$

To compute the prior on the large separation, at least five modes of angular degree l are needed. For this reason, the prior on the large separation is only applied when this condition is met. The prior on the small separation is only applied to $d\nu_{0,2}(n)$, which was found to be enough for a stable fit (Davies et al. 2016).

Mode line widths. For the mode line widths, we apply a uniform prior with lower and upper limits of 0 and 12 μHz.

Mode heights. We also apply a uniform prior on the height of the radial modes, whose lower limit is fixed at 0 ppm^2/μHz and whose upper limit varies from power spectrum to power spectrum, estimated as follows:

1. the frequency range of interest, the p-mode envelope, is defined as $[\nu_-^0 - \Delta\nu/4, \nu_+^0 + \Delta\nu/4]$, where ν_-^0 and ν_+^0 are the minimum and maximum mode frequencies we consider (again, 0 denotes the values from the literature);
2. the contribution of the acoustic background is removed from the power spectrum;
3. the resulting power spectrum is smoothed by applying a uniform filter with a size equal to the reciprocal of the resolution of the spectrum; and
4. the height upper limit is defined as the maximum height of the smoothed power spectrum.

Stellar rotational splitting and inclination angle. We use the posterior distributions obtained in previous studies (based on the complete light curves) by Davies et al. (2016) and Lund et al. (2017) as priors on the stellar rotational splitting and stellar inclination angle.

2.5.2. Fitting Method

The global fit to the acoustic modes is performed through implementation of the algorithm `emcee` (Foreman-Mackey et al. 2013), based on the Affine Invariant MCMC Ensemble sampler (Goodman & Weare 2010). `emcee` makes use of an interacting ensemble of so-called "walkers." Each walker has its own separate MCMC chain but the proposal distribution, i.e., the next step in the chain, depends on the positions of the remaining walkers. Furthermore, in order to ensure an efficient sampling of the parameter space, we also employ parallel tempering (Earl & Deem 2005), which is useful to avoid cases where a given walker gets trapped in a local maximum and to access broader regions of the parameter space.

For each power spectrum, we use 500 walkers (initialized by sampling the prior distributions) and three temperatures defined according to Benomar et al. (2009). Each chain runs for 10^4 steps after a burn-in phase, long enough to ensure the convergence of the chains and a swap acceptance rate between adjacent temperatures of about 50%.

For each model parameter, the posterior distribution is obtained by computing the histogram of its sampled values. The final parameter estimates and uncertainties are based on the 16th, 50th, and 84th percentiles, i.e., given by the median and the 68% credible region of the distribution.

2.6. Mean Frequency Shift and Mean Height Estimation

In order to search for temporal variations of the acoustic mode frequencies, the original time-series are divided into 90-day sub-series overlapped by 45 days (in average, 22 sub-series per star).

With the mode frequencies, ν_{nl}, and the respective uncertainties (obtained with the peak-bagging tool described above) for each sub-series, one can then estimate the temporal frequency shifts. The reference mode frequencies, ν_{nl}^{ref}, are taken as the weighted time averages of the mode frequencies. Then, for each multiplet (n, l), we compute the variation in frequency with respect to the reference frequencies as

$$\delta\nu_{nl}(t) = \nu_{nl}(t) - \nu_{nl}^{\mathrm{ref}}. \tag{13}$$

Finally, following the approach used by, e.g., Chaplin et al. (2007) and Tripathy et al. (2007), we obtain the weighted mean frequency shifts as

$$\delta\nu(t) = \frac{\sum_{nl}\delta\nu_{nl}(t)/\sigma_{nl}^2(t)}{\sum_{nl}1/\sigma_{nl}^2(t)}. \tag{14}$$

The uncertainties on the mean frequency shifts are

$$\sigma(t) = \left(\sum_{nl}\frac{1}{\sigma_{nl}^2(t)}\right)^{-1/2}. \tag{15}$$

Note that for the low-degree modes, the mode inertia dependency on the angular degree is not significant (e.g., Chaplin et al. 2007) therefore we have neglected the inertia ratio in the frequency shift estimation.

In the Sun, the acoustic frequencies and heights show an anti-correlated behavior with time: while the frequencies increase with increasing activity level, the mode heights decrease. Evidence for such anti-correlated behavior was also found in solar-type stars observed by *CoRoT* and *Kepler* (García et al. 2014; Kiefer et al. 2017). Therefore, we also search for temporal variations in the latter.

The mode height distributions follow a log-normal distribution. For this reason, we use the logarithm of the mode heights in the calculations for the mean height estimates. Thus, the mean logarithmic heights are computed as the weighted average of the logarithm of the mode heights, following the same approach used for the frequency shifts, i.e.

$$\ln S(t) = \frac{\sum_n \ln S_{n0}(t)/\sigma_{\ln S_{n0}}^2(t)}{\sum_n 1/\sigma_{\ln S_{n0}}^2(t)}, \tag{16}$$
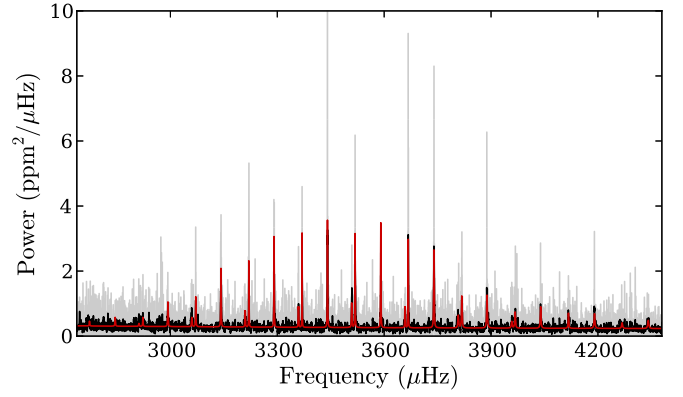
Figure 4. Power-density spectrum (gray and black; with different smoothings for illustrative purposes) for a given 90-day sub-series of the solar-type star KIC 8006161. The red lines show the best fit to the power spectrum obtained with the Bayesian peak-bagging tool.

$$\sigma_S(t) = \left(\sum_n \frac{1}{\sigma_{\ln S_{n0}}^2(t)}\right)^{-1/2}. \tag{17}$$

3. Peak-bagging Analysis

Before applying the peak-bagging tool to the *Kepler* data, we validated the tool with real and artificial solar data. The results from the validation tests are shown in Appendix A. This section presents the results for the *Kepler* targets.

Considering the background model, obtained in Section 2.4, for each 90-day sub-series for each star, we apply the peak-bagging tool as described in Section 2.5, obtaining the marginal posterior probability distributions for the model parameters.

The final parameter estimates are given by the median of the posterior probability distribution and the uncertainties are determined based on the 68% credible region (see Section 2.5.2). Figure 4 compares the power spectrum and the best fit obtained with the peak-bagging tool for a given sub-series of one of the stars in the sample (KIC 8006161).

3.1. Mean Frequency Shifts and Mode Heights

With the mode frequencies for each sub-series, we then compute the weighted mean frequency shifts over time for each star (see Section 2.6 for details). We compare them with frequency shifts that we obtained with the cross-correlation method that is described in detail in Kiefer et al. (2017). With this method, estimates of the frequency shifts and the corresponding uncertainties are obtained in the following way: first, 200 realizations of the time-series of each segment are generated with a resampling approach and their period-ograms are calculated. Subsequently, the p-mode frequency-range of the periodograms of each segment are cross-correlated with the p-mode frequency-range of the periodograms of the reference segment. The resulting cross-correlation functions (CCFs) are fitted with a Lorentzian profile. The mean of the centroids of the 200 Lorentzian fits is used as the value for the frequency shift and the standard deviation of the centroids is used as the uncertainty.

The top panel of Figure 5 compares the frequency shifts obtained with the Bayesian peak-bagging tool with those from the cross-correlation method for the solar-type star KIC 8006161. The frequency shifts presented here are obtained while considering only the five central orders (closest to ν_{max}),
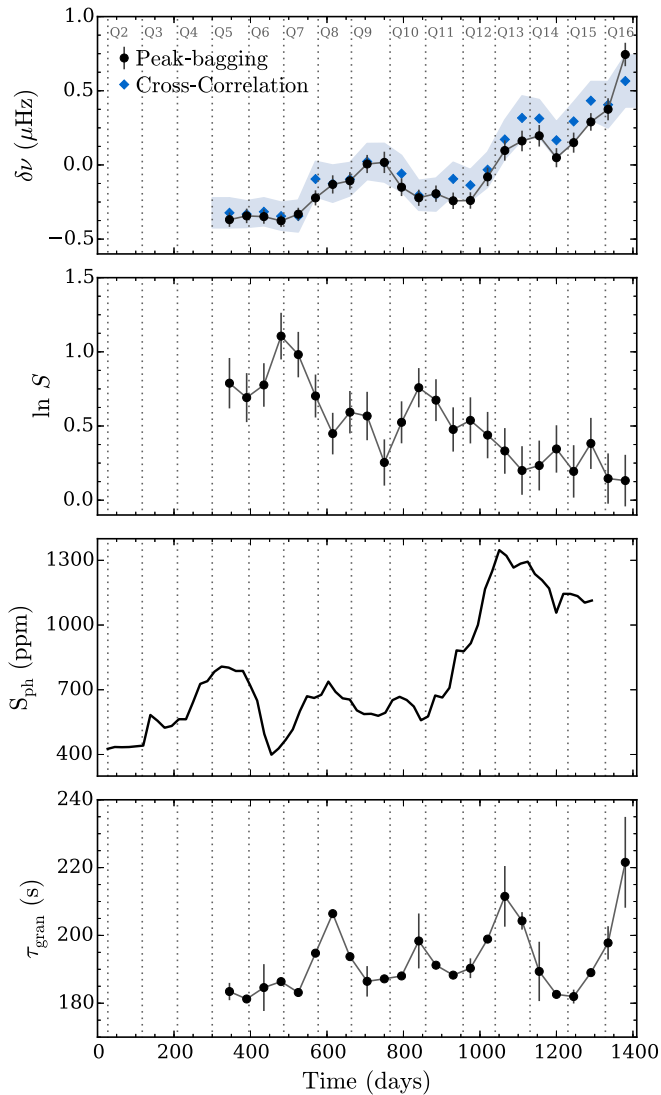
Figure 5. Results for the solar-type star KIC 8006161. Top panel: comparison between the mean frequency shifts obtained with the Bayesian peak-bagging tool (black) and the cross-correlation method (blue; method described in Kiefer et al. 2017). Second panel: logarithmic mode height obtained from the peak-bagging analysis. Third panel: photometric magnetic activity proxy. Bottom panel: characteristic timescale of the granulation. Vertical dotted lines mark the start/end of *Kepler* quarters.

which usually have the largest signal-to-noise ratio in the p-modes. Note that the frequency shifts derived from our method are relative to the average value (see Section 2.6), while the frequency shifts from the cross-correlation method are estimated in relation to the first sub-series. Therefore, the latter are displaced by their average value in Figure 5. First, this comparison shows that the results obtained with both methods agree very well. Second, the uncertainties on the estimated frequency shifts are smaller by a factor of a few when employing the peak-bagging method.[9] This reassures us that our peak-bagging tool is able to successfully recover accurate mode frequencies, and consequently, their temporal variations. Table 2 lists the results for KIC 8006161.

In the Sun, the amplitude of the acoustic modes is also observed to vary over the solar cycle (e.g., Elsworth et al. 1993; Chaplin et al. 2000; Salabert & Jiménez-Reyes 2006; Howe et al. 2015), decreasing with increasing magnetic activity. Thus, the acoustic frequencies and amplitudes show an anti-correlated temporal variation over the solar cycle.

Assuming that the underlying magnetically induced changes in other solar-type stars are similar to those in the Sun, evidence of an anti-correlated behavior between the acoustic frequencies and heights may be an important aspect to confirm the activity-related origin of the observed variations. With this in mind, we also searched for temporal variations in the mode heights. However, we note that this seismic indicator is not expected to be as robust as the frequency shifts.

The second panel of Figure 5 shows the temporal evolution of the weighted average of the logarithmic mode heights estimated with the peak-bagging tool for KIC 8006161 (see Section 2.6), while the third panel of Figure 5 shows the photometric magnetic activity proxy, $S_{\rm ph}$ (see Section 2.3). These results suggest that the acoustic mode frequencies of KIC 8006161 (top panel) increase with increasing activity level, while the mode heights experience a decrease, which resembles what is observed for the Sun. Also, the behavior of the mode heights is in good agreement with that found for the height of the p-mode envelope by Kiefer et al. (2017).

In order to access the correlation between the different quantities and to account for possible temporal offsets, we compute the CCF between the frequency shifts and the remainder quantities. As an example, the results for the CCF for KIC 8006161 are shown in Figure 6. The top panel of Figure 6 shows the CCF between the mean frequency shifts and the mean logarithmic mode heights. The black symbols concern the results obtained while considering all the data points, i.e., all the 90-day sub-series. The blue and red symbols concern the two sub-samples of independent data points, i.e., while considering every two sub-series of 90 days. For reference, the 95% significance levels are marked. The results show that the anti-correlation between frequency shifts and mode heights is significant (the absolute value is above the 95% significance level). The maximum anti-correlation is found at 0-Lag. The middle panel of Figure 6 shows the CCF between the frequency shifts and the interpolated photometric activity proxy (interpolated at the same times as the $\delta\nu$). The results suggest a strong correlation between the temporal frequency shifts and the photometric activity and the maximum correlation is found at 0-Lag. Table 3 summarizes the results from the cross-correlation between the frequency shifts and the remaining quantities for all stars in the sample. For simplification, only the results for all the data points are listed. Also, in the table we consider temporal lags between ±90 days and we list the maximum absolute correlation within those temporal lags and the corresponding lag.

3.2. On the Relation between Frequency Shifts and the Granulation Timescale

Although it is still a matter of debate in the literature, the properties of the solar granulation, namely amplitude and characteristic timescale, may be affected by magnetic activity. Muller et al. (2007) found evidence for a decrease in the granulation amplitude with increasing activity. However, other studies found no significant variation in this parameter (Pallé et al. 1995; Régulo et al. 2002, 2005; Lefebvre et al. 2008;

---

[9] For stars common to both studies, the uncertainties on the frequency shifts obtained through the cross-correlation method presented here are larger than those in Kiefer et al. (2017) due to the length of the sub-series, which is shorter for this work.

Table 2
Results for the Solar-type Star KIC 8006161

				KIC 8006161				
			Peak-bagging					Cross-correlation
Time (days)	Duty Cycle	τ_{gran} (s)	$\delta\nu_{l=0}$ (μHz)	$\delta\nu_{l=1}$ (μHz)	$\delta\nu_{l=2}$ (μHz)	$\delta\nu$ (μHz)	ln S	$\delta\nu$ (μHz)
345	0.97	183.4 ± 2.6	−0.38 ± 0.06	−0.35 ± 0.07	−0.32 ± 0.13	−0.37 ± 0.05	0.79 ± 0.17	−0.32 ± 0.10
390	0.97	181.2 ± 0.3	−0.26 ± 0.07	−0.45 ± 0.07	−0.44 ± 0.15	−0.34 ± 0.05	0.69 ± 0.17	−0.33 ± 0.09
435	0.96	184.6 ± 6.9	−0.32 ± 0.06	−0.39 ± 0.08	−0.45 ± 0.14	−0.35 ± 0.05	0.78 ± 0.15	−0.32 ± 0.09
480	0.97	186.4 ± 0.2	−0.35 ± 0.05	−0.43 ± 0.07	−0.30 ± 0.12	−0.38 ± 0.04	1.11 ± 0.16	−0.35 ± 0.09
525	0.96	183.2 ± 0.6	−0.28 ± 0.05	−0.44 ± 0.08	−0.36 ± 0.12	−0.33 ± 0.04	0.98 ± 0.15	−0.34 ± 0.11
570	0.80	194.8 ± 0.6	−0.22 ± 0.06	−0.23 ± 0.09	−0.17 ± 0.15	−0.22 ± 0.05	0.70 ± 0.14	−0.10 ± 0.12
615	0.78	206.4 ± 0.4	−0.10 ± 0.08	−0.17 ± 0.09	−0.13 ± 0.18	−0.13 ± 0.06	0.45 ± 0.14	−0.13 ± 0.13
660	0.89	193.7 ± 0.0	−0.03 ± 0.08	−0.21 ± 0.09	−0.14 ± 0.17	−0.11 ± 0.06	0.59 ± 0.14	−0.10 ± 0.11
705	0.93	186.5 ± 4.5	0.12 ± 0.09	−0.10 ± 0.09	−0.12 ± 0.17	0.01 ± 0.06	0.57 ± 0.16	0.02 ± 0.12
750	0.97	187.2 ± 0.2	0.16 ± 0.10	−0.13 ± 0.10	−0.18 ± 0.14	0.02 ± 0.07	0.25 ± 0.16	0.01 ± 0.13
795	0.97	188.0 ± 0.3	−0.16 ± 0.08	−0.14 ± 0.09	−0.35 ± 0.15	−0.15 ± 0.06	0.52 ± 0.14	−0.06 ± 0.12
840	0.98	198.4 ± 8.1	−0.12 ± 0.07	−0.40 ± 0.09	−0.57 ± 0.15	−0.22 ± 0.05	0.76 ± 0.13	−0.20 ± 0.10
885	0.94	191.2 ± 0.3	−0.18 ± 0.07	−0.22 ± 0.09	−0.69 ± 0.13	−0.19 ± 0.06	0.67 ± 0.14	−0.20 ± 0.11
930	0.92	188.3 ± 0.8	−0.33 ± 0.07	−0.10 ± 0.09	−0.17 ± 0.18	−0.24 ± 0.06	0.48 ± 0.15	−0.09 ± 0.11
975	0.90	190.3 ± 2.9	−0.27 ± 0.07	−0.20 ± 0.09	−0.05 ± 0.14	−0.24 ± 0.06	0.54 ± 0.16	−0.14 ± 0.11
1020	0.90	198.9 ± 0.2	−0.09 ± 0.09	−0.07 ± 0.09	0.00 ± 0.15	−0.08 ± 0.06	0.44 ± 0.16	−0.03 ± 0.12
1065	0.95	211.5 ± 8.9	0.06 ± 0.09	0.15 ± 0.11	−0.30 ± 0.17	0.10 ± 0.07	0.33 ± 0.15	0.17 ± 0.13
1110	0.89	204.3 ± 2.6	0.12 ± 0.09	0.23 ± 0.11	−0.01 ± 0.22	0.16 ± 0.07	0.20 ± 0.16	0.32 ± 0.15
1155	0.89	189.4 ± 8.7	0.12 ± 0.11	0.25 ± 0.09	0.39 ± 0.18	0.20 ± 0.07	0.23 ± 0.17	0.31 ± 0.13
1200	0.95	182.6 ± 0.9	−0.03 ± 0.09	0.14 ± 0.10	0.21 ± 0.14	0.05 ± 0.06	0.35 ± 0.16	0.17 ± 0.12
1245	0.90	182.0 ± 2.0	0.09 ± 0.09	0.22 ± 0.10	0.38 ± 0.17	0.15 ± 0.07	0.19 ± 0.18	0.29 ± 0.13
1290	0.89	189.0 ± 0.0	0.13 ± 0.08	0.51 ± 0.09	0.49 ± 0.20	0.29 ± 0.06	0.38 ± 0.17	0.43 ± 0.13
1335	0.84	197.8 ± 4.9	0.21 ± 0.10	0.59 ± 0.11	0.47 ± 0.23	0.38 ± 0.07	0.15 ± 0.17	0.41 ± 0.16
1380	0.84	221.6 ± 13.4	0.78 ± 0.09	0.65 ± 0.15	0.80 ± 0.18	0.74 ± 0.08	0.13 ± 0.17	0.57 ± 0.17

Note. Column 1: time of the sub-series midpoint relative to the starting time of the observations. Column 2: duty-cycle for each sub-series. Column 3: characteristic timescale of the granulation component. Columns 4-8: mean frequency shifts (for radial ($\delta\nu_{l=0}$), dipolar ($\delta\nu_{l=1}$), and quadrupolar ($\delta\nu_{l=2}$) modes, and when combining the $l = 0$ and $l = 1$ modes ($\delta\nu$)) and logarithmic mode heights obtained from the Bayesian peak-bagging analysis. Note that the results presented here are based on the five central orders (see the text); in particular, for KIC 8006161, we use modes of radial order ranging between 19 and 23. Column 9: frequency shifts obtained with the cross-correlation method described in Kiefer et al. (2017).

(This table is available in its entirety in machine-readable form.)

Karoff 2012). Regarding the granulation characteristic time-scale, while Lefebvre et al. (2008) claim no significant variation, Régulo et al. (2002, 2005) found that the granulation timescale increases with increasing activity. Moreover, although Lefebvre et al. (2008) and Karoff (2012) found that the granulation properties are mostly independent of the 11 years solar cycle, these authors found evidence for shorter quasi-periodic (∼1 year) variations, whose origin is still not understood. Lefebvre et al. (2008), however, related those variations to instrumental effects.

For stars other than the Sun, the relation between magnetic activity and the granulation properties is also not clear. García et al. (2010) found no correlation between the observed activity-related frequency shifts and the granulation timescale for the solar-type star HD 49933 observed by *CoRoT*. Karoff et al. (2013a) analyzed the variability of the granulation component on three solar-type stars observed by *Kepler*. For two of these stars (KIC 6603624 and KIC 6933899, both in our sample), the authors found quasi-annual/biennial periodicities on the granu-lation parameters that resemble the quasi-biennial variations in the different solar activity indicators (Bazilevskaya et al. 2014; McIntosh et al. 2015; Salabert et al. 2017), including frequency shifts (Fletcher et al. 2010; Broomhall et al. 2012; Broomhall & Nakariakov 2015). Finally, Kiefer et al. (2017) did not find evidence for a systematic correlation between the granulation

timescale and the frequency shifts for their sample of 24 solar-type stars.

With the above in mind, we have been searching for correlations between the frequency shifts obtained using the Bayesian peak-bagging tool and the granulation characteristic timescale obtained in Section 2.4.

The bottom panel of Figure 5 shows the characteristic timescale of the granulation, τ_{gran}, over time for KIC 8006161. For this star the granulation timescale and the frequency shifts do not appear to have a correlated behavior. However, some of the variations seen in the granulation timescale may be related to local variations in the acoustic frequencies (top panel).

The bottom panel of Figure 6 shows the cross-correlation between the mean frequency shifts and the granulation timescale as a function of the lag between the two observables. These results indicate that there is a significant correlation (above the 95% significance level) between frequency shifts and granulation timescale in the case of all data points (black) and for one sample of independent data points (shown in red). The maximum correlation is found at 0-Lag.

From the 87 solar-type stars analyzed in this work, 31 stars exhibit a significant (above the 95% significance level) correlation or anti-correlation between the observed frequency shifts and the granulation timescale. In the next subsection, we highlight the results for five additional stars (besides KIC 8006161).
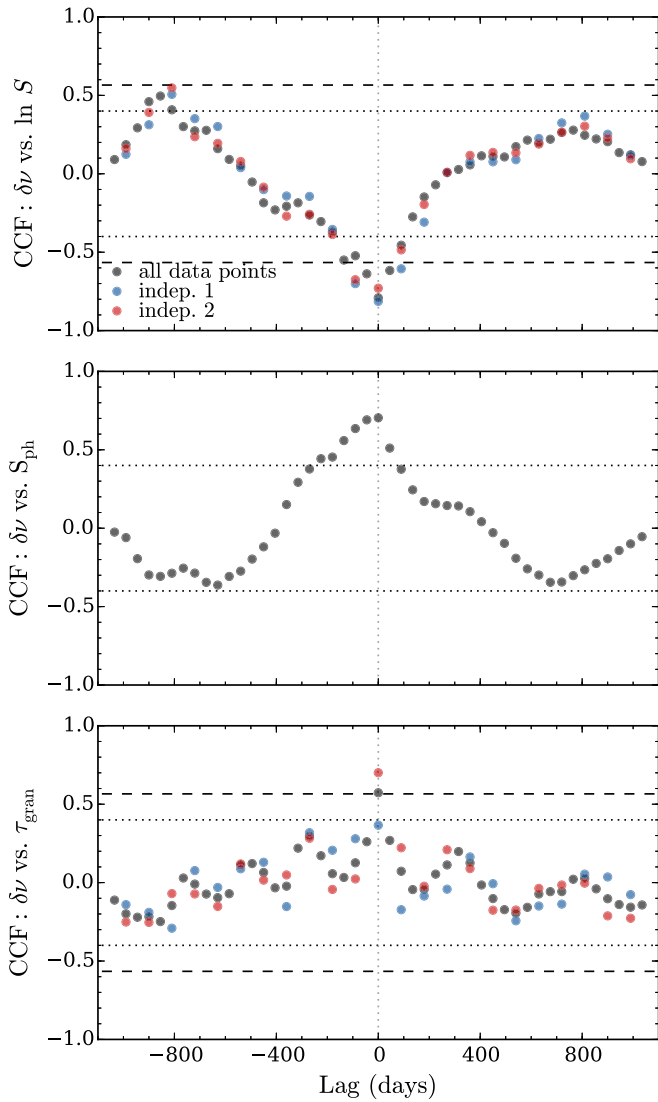
Figure 6. CCF results for KIC 8006161, displaying the cross-correlation function between frequency shifts and logarithmic mode heights (top panel); interpolated photometric activity proxy (middle panel); and characteristic granulation timescale (bottom panel). The black symbols correspond to the results for all the data points, while the blue and red symbols show the results for the independent data points. The horizontal dotted and dashed lines mark the 95% significance levels for all data points and the independent data points, respectively. The dotted vertical lines indicate the 0-Lag.

3.3. Results for the Whole Sample

The results from our analysis indicate that activity-related variations in the acoustic frequencies are likely a common phenomenon among solar-type stars. We find evidence for quasi-periodic variations in about 60% of the targets. Among those, more than 70% show variations in other activity indicators: in the logarithmic mode heights, in the photometric activity proxy, and/or in the granulation timescale. The detailed results for the complete target sample are presented in Appendix B.

We note that for some of the analyzed targets we find (quasi-)periodic variations in the frequency shifts and/or in the background parameters with a period close to *Kepler*'s orbital period (i.e., close to 372.5 days). For those, one must be careful in the interpretation of the results. Similar behavior is found with different calibrated data: KASOC (Handberg & Lund

2014); KADACS (García et al. 2011); and PDC-MAP (Presearch Data Conditioning—Maximum A Posteriori; Smith et al. 2012; Stumpe et al. 2012). Therefore, those periodicities should not result from an artifact introduced during the preparation of the light curves. Also, they are found with both the peak-bagging and cross-correlation methods. From those cases, we highlight the solar-type stars KIC 9139163 and KIC 6933899. The results for KIC 9139163 show periodic variations in the frequency shifts and characteristic granulation timescale with a period consistent with *Kepler*'s orbital period. For KIC 6933899, we find periodic variations with similar period in the granulation timescale, granulation amplitude, and in the frequency shifts. The frequency shifts are ahead in time in relation to the granulation parameters. The granulation component of this star was previously analyzed by Karoff et al. (2013a).[10] Based on 13-month time-series, the authors found a temporal variation in the granulation timescale with a period of ∼233 days. Here, based on a time-series three times longer, we also find a temporal variation in the granulation parameters, but with a different periodicity consistent with *Kepler*'s orbital period. Although less clear than the highlighted cases, another three stars (KIC 1435465, KIC 8077137, and KIC 8179536) also show evidence for variations in the acoustic frequencies with the same periodicity. If we neglect these cases, the previously indicated percentage of stars with significant frequency shifts does not change, as we used rounded numbers.

In what follows, we present the results for five additional solar-type stars (besides KIC 8006161) that show evidence for activity-related frequency shifts.

3.3.1. KIC 5184732

Figure 7 presents the results for KIC 5184732. In general, the mean frequency shifts (top panel) increase over time, while the mean mode heights (second panel) experience a decrease. This is consistent with the two quantities being anti-correlated in time, similar to the Sun and KIC 8006161. The results from the CCF (Table 3) confirm the anti-correlation between the mean frequency shifts and mode heights. Furthermore, the variation in the photometric activity proxy (S_{ph}; third panel of Figure 7) is consistent with the variation in the frequency shifts. In fact, these two quantities are strongly correlated (Table 3). The full S_{ph} time-series suggests a cyclic behavior in the surface magnetism, showing what resembles the end of a cycle and the beginning of a new cycle.

For the characteristic granulation timescale, our results (bottom panel of Figure 7 and Table 3) suggest that there is no significant temporal variation and correlation with the frequency shifts.

Finally, the results shown in the two top panels of Figure 7 are consistent with those in Kiefer et al. (2017).

3.3.2. KIC 9414417 (KOI 974)

Figure 8 presents the results for KIC 9414417. We find quasi-periodic variations in the frequencies (top panel) and logarithmic heights (second panel) of the acoustic modes. However, for KIC 9414417, the mode frequencies and heights vary in phase, while in the Sun, these two properties vary in

---

[10] Karoff et al. (2013a) also found a periodic variability on the granulation component of KIC 6603624 with a period of ∼322 days. In this work, based on a longer time-series, we find the granulation parameters varying with a shorter periodicity of ∼225 days.

Table 3
Summary of the Results from the Cross-correlation Function between Frequency Shifts and Logarithmic Mode Heights (Columns 2 and 3), Frequency Shifts and Interpolated Photometric Activity Proxy (Columns 4 and 5), and Frequency Shifts and Granulation Timescale (Columns 6 and 7)

| KIC | $\delta\nu$ versus $\ln S$ | | $\delta\nu$ versus $S_{\rm ph}$ | | $\delta\nu$ versus $\tau_{\rm gran}$ | | 95% |
	CCF Value	Lag	CCF Value	lag	CCF Value	Lag	Significance Level
1435467	−0.603	90	−0.266	−90	0.380	0	±0.400
2837475	−0.149	45	−0.217	0	0.344	90	±0.400
3425851	−0.557	90	⋯	⋯	0.899	0	±0.980
3427720	−0.473	0	0.262	0	0.424	0	±0.400
3456181	0.468	0	⋯	⋯	−0.526	45	±0.524
3544595	0.153	90	⋯	⋯	−0.207	−90	±0.358
3632418	0.270	−90	−0.457	−45	0.356	−90	±0.400
3656476	0.435	90	0.365	−90	−0.190	45	±0.400
3735871	−0.352	−90	0.347	0	−0.501	45	±0.400
4141376	−0.374	0	⋯	⋯	0.159	−45	±0.418
4349452	0.333	0	⋯	⋯	−0.566	−90	±0.400
4914423	0.371	90	⋯	⋯	0.272	−90	±0.438
4914923	0.281	45	0.322	45	−0.527	45	±0.400
5184732	−0.482	90	0.689	45	−0.379	0	±0.438
5773345	0.586	−90	0.371	−45	0.470	−90	±0.591
5866724	0.279	45	⋯	⋯	−0.467	45	±0.370
5950854	0.662	45	⋯	⋯	−0.514	−90	±0.566
6106415	−0.508	90	⋯	⋯	−0.442	45	±0.428
6116048	0.312	−90	0.137	45	−0.546	90	±0.400
6225718	0.496	90	⋯	⋯	0.444	−45	±0.418
6278762	0.987	0	⋯	⋯	−0.961	45	±0.980
6508366	0.663	0	−0.305	45	0.368	0	±0.400
6521045	0.491	90	⋯	⋯	−0.318	−90	±0.370
6603624	0.532	90	⋯	⋯	−0.432	−90	±0.400
6679371	0.417	0	−0.502	0	−0.154	−90	±0.400
6933899	−0.637	−45	⋯	⋯	0.442	45	±0.400
7103006	−0.468	0	0.325	−45	0.574	45	±0.400
7106245	−0.329	45	⋯	⋯	0.413	−90	±0.418
7206837	0.278	45	−0.192	90	0.170	90	±0.400
7296438	0.617	45	−0.534	−90	0.625	0	±0.620
7510397	0.664	0	⋯	⋯	0.257	90	±0.438
7670943	0.526	0	⋯	⋯	0.334	45	±0.418
7680114	0.442	45	−0.438	0	−0.308	−90	±0.400
7771282	0.728	45	0.438	0	−0.805	0	±0.524
7871531	0.303	−90	0.325	0	0.152	90	±0.400
7940546	−0.285	−90	−0.642	−45	0.236	90	±0.438
7970740	−0.369	0	0.481	−90	−0.524	45	±0.418
8006161	−0.791	0	0.704	0	0.573	0	±0.400
8077137	−0.398	90	⋯	⋯	−0.317	90	±0.418
8150065	−0.407	45	⋯	⋯	−0.512	45	±0.566
8179536	0.623	0	−0.254	90	−0.691	0	±0.524
8228742	0.424	0	0.643	45	0.618	−45	±0.400
8292840	−0.561	−45	⋯	⋯	−0.575	90	±0.400
8379927	0.508	0	0.299	0	0.400	−45	±0.392
8394589	−0.583	0	⋯	⋯	−0.463	−45	±0.400
8424992	−0.535	90	⋯	⋯	0.483	90	±0.693
8478994	−0.700	−90	⋯	⋯	0.345	90	±0.400
8494142	−0.228	−45	⋯	⋯	−0.394	−90	±0.438
8694723	−0.365	90	0.436	−45	−0.442	0	±0.400
8760414	−0.475	45	⋯	⋯	−0.112	−45	±0.400
8866102	−0.421	90	⋯	⋯	0.354	0	±0.370
8938364	−0.360	0	⋯	⋯	−0.274	45	±0.418
9025370	0.383	0	0.347	0	−0.569	45	±0.400
9098294	−0.440	45	0.196	−45	−0.379	45	±0.400
9139151	0.510	0	0.355	0	0.386	45	±0.400
9139163	−0.396	0	0.401	90	0.543	0	±0.400
9206432	0.653	45	0.418	0	−0.362	−90	±0.490
9353712	0.445	−45	0.258	0	0.220	−45	±0.490
9410862	0.466	45	0.488	0	0.444	0	±0.418
9414417	0.452	−45	0.221	45	0.675	45	±0.428
9592705	0.330	45	⋯	⋯	0.409	−90	±0.418
9812850	−0.215	−90	0.235	−90	0.336	90	±0.400

Table 3
(Continued)

KIC	$\delta\nu$ versus $\ln S$		$\delta\nu$ versus $S_{\rm ph}$		$\delta\nu$ versus $\tau_{\rm gran}$		95% Significance Level
	CCF Value	Lag	CCF Value	lag	CCF Value	Lag	
9955598	−0.317	−90	0.141	−90	0.171	0	±0.400
9965715	−0.298	45	…	…	0.538	0	±0.462
10068307	−0.719	90	−0.282	90	0.306	−90	±0.438
10079226	−0.357	90	0.467	0	−0.250	90	±0.693
10162436	0.560	0	0.255	−90	−0.742	0	±0.418
10454113	−0.374	0	−0.270	−45	0.210	90	±0.400
10516096	−0.251	−45	…	…	−0.612	0	±0.400
10586004	0.893	0	…	…	0.896	0	±0.980
10644253	−0.178	45	0.347	0	0.159	90	±0.400
10666592	0.378	0	…	…	−0.243	90	±0.346
10730618	−0.516	45	…	…	−0.329	45	±0.438
10963065	−0.394	0	0.264	0	−0.049	0	±0.392
11081729	−0.257	0	0.477	−45	−0.187	0	±0.400
11253226	0.401	−45	−0.076	−90	−0.252	−45	±0.400
11295426	−0.425	90	…	…	−0.449	90	±0.400
11401755	0.692	0	…	…	−0.479	−45	±0.418
11772920	0.270	−90	…	…	0.294	45	±0.400
11807274	0.426	0	…	…	0.364	−45	±0.418
11904151	0.217	−45	…	…	0.262	−45	±0.358
12009504	0.297	0	0.169	90	0.369	90	±0.400
12069127	−0.181	−45	0.365	45	−0.384	45	±0.524
12069424	−0.197	−90	…	…	0.132	45	±0.438
12069449	0.785	0	…	…	−0.341	90	±0.438
12258514	−0.531	−90	0.427	0	0.306	−90	±0.400
12317678	−0.197	−45	…	…	0.119	90	±0.400

Note. Column 1 lists the KIC numbers of the targets. The CCF values (columns 2, 4, and 6) correspond to the maximum absolute CCF values within the temporal lags ±90 days, and the respective lag is shown in columns 3, 5, and 7. For reference, the 95% significance levels are in column 8.

anti-phase over the solar activity cycle. The results from the CCF show that the correlation between frequency shift and mode heights is significant (Table 3).

Interestingly, the characteristic timescale of the granulation (bottom panel of Figure 8) also shows a quasi-periodic modulation with a temporal offset in relation to the variation in the seismic properties. The granulation timescale and frequency shifts are strongly correlated (Table 3).

Knowing that the inclination angle of KIC 9414417 is close to 90° (e.g., Campante et al. 2016) and assuming a spot latitudinal distribution similar to that in the Sun, the photometric activity proxy (third panel of Figure 8) thus suggests relatively weak photometric activity for this star. Still, there are two epochs of large $S_{\rm ph}$ that coincide with epochs of large frequency shifts.

3.3.3. KIC 10644253

Salabert et al. (2016b) found evidence for activity-related frequency shifts in KIC 10644253, which vary in agreement with the photometric activity proxy, $S_{\rm ph}$. Later, Kiefer et al. (2017) confirmed the temporal variation in the acoustic frequencies of this star.

The solar-type star KIC 10644253 is also part of the target sample analyzed in this work. The black symbols in the two top panels of Figure 9 show the frequency shifts and logarithmic mode heights derived from the peak-bagging analysis (Section 2). For comparison, the frequency shifts computed with the cross-correlation method, described in Kiefer et al. (2017), are shown in blue in the top panel of

Figure 9. In spite of the large errors associated with the cross-correlation method, the frequency shifts obtained with the two methods are still in good agreement. Moreover, the results from the peak-bagging analysis are in good agreement with those in the literature (Salabert et al. 2016b; Kiefer et al. 2017). Therefore, our analysis further confirms the temporal frequency shifts in KIC 10644253, which show a similar behavior to that of the photometric activity proxy (third panel of Figure 9). Also, the CCF results show that frequency shifts and $S_{\rm ph}$ are correlated. However, the correlation is below the 95% significance level.

For the mode heights (second panel of Figure 9) we do not find a significant variation. However, from the CCF (Table 3) there is some evidence for an anti-correlation between the frequency shifts and the mode heights.

The bottom panel of Figure 9 shows the granulation timescale (estimated as described in Section 2.4). For this star in particular, the variations in the acoustic frequencies and in the photometric proxy are similar to that in the characteristic timescale of the granulation. In spite of the relatively low significance, the CCF between the frequency shifts and the granulation timescale (Table 3) suggests that the variations in these two properties are correlated.

3.3.4. KIC 7970740

Figure 10 displays the results for the solar-type star KIC 7970740. The frequency shifts obtained with the peak-bagging analysis (black symbols in the top panel) increase slightly over time and agree reasonably well with those from
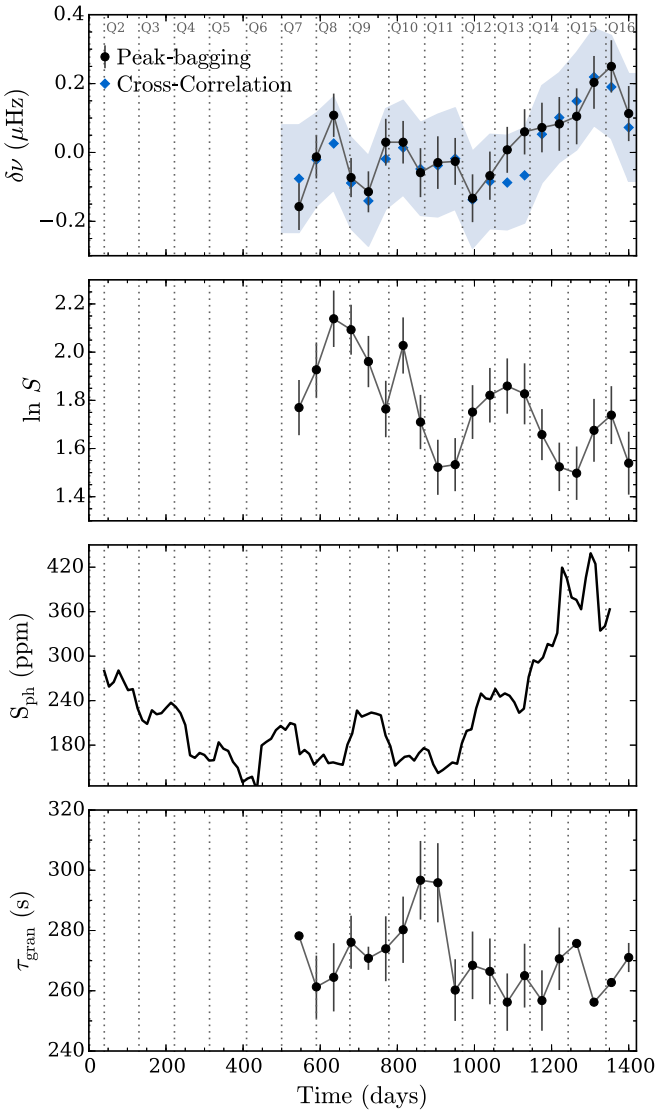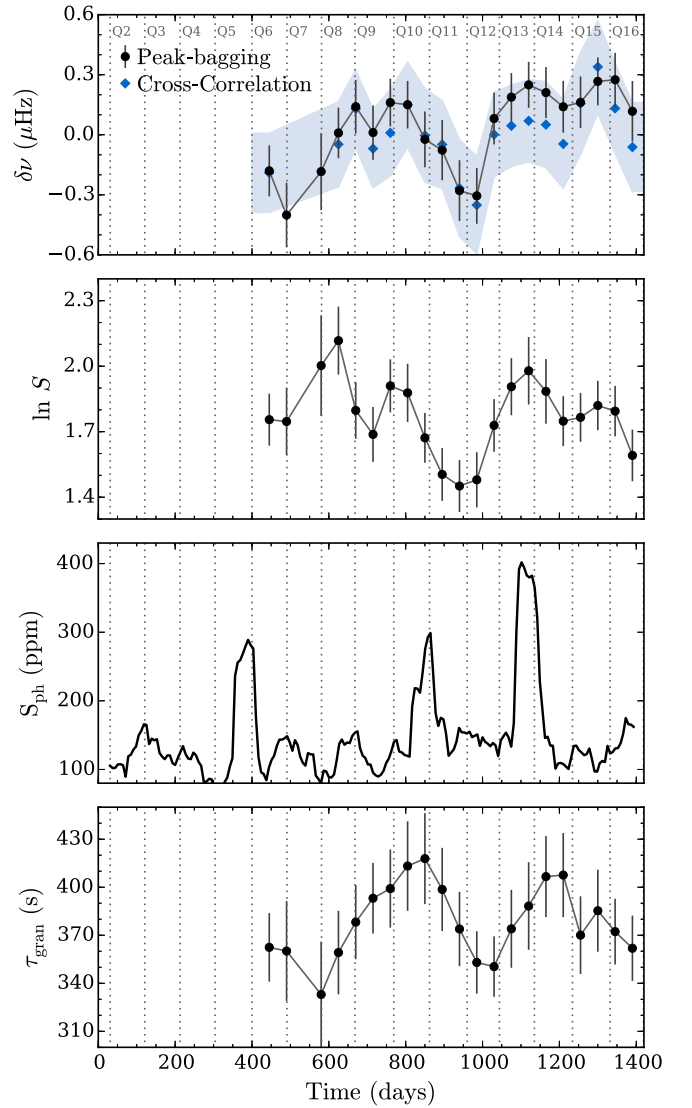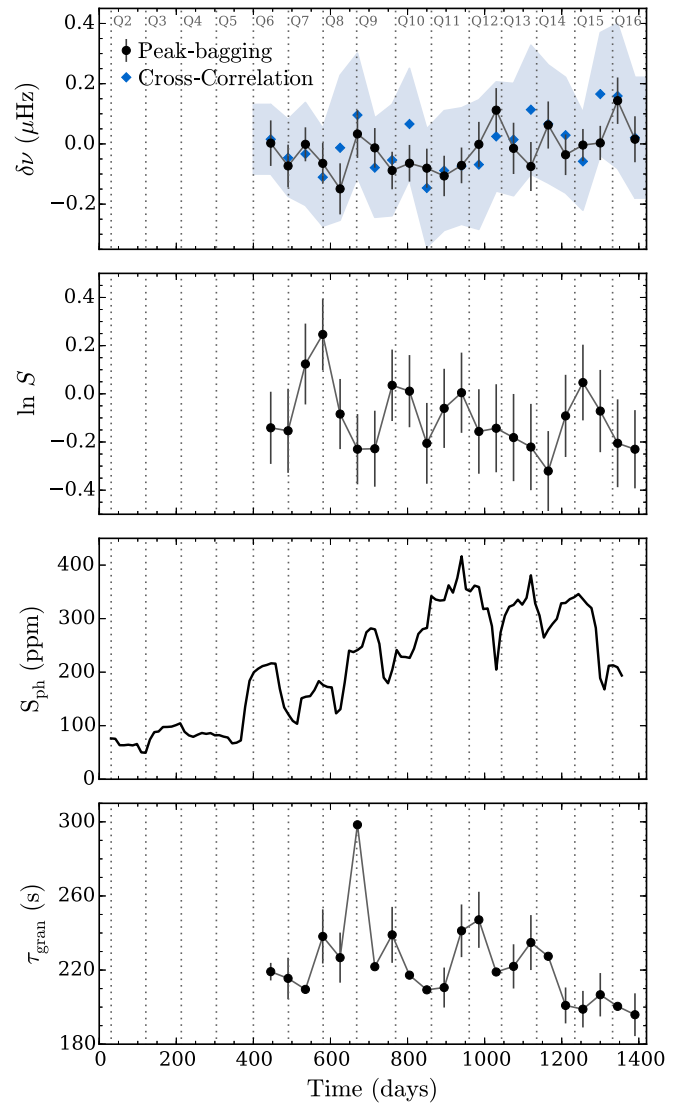
Figure 7. Results for KIC 5184732 (same as in Figure 5): mean frequency shifts, mode heights, photometric activity proxy, and characteristic granulation timescale.
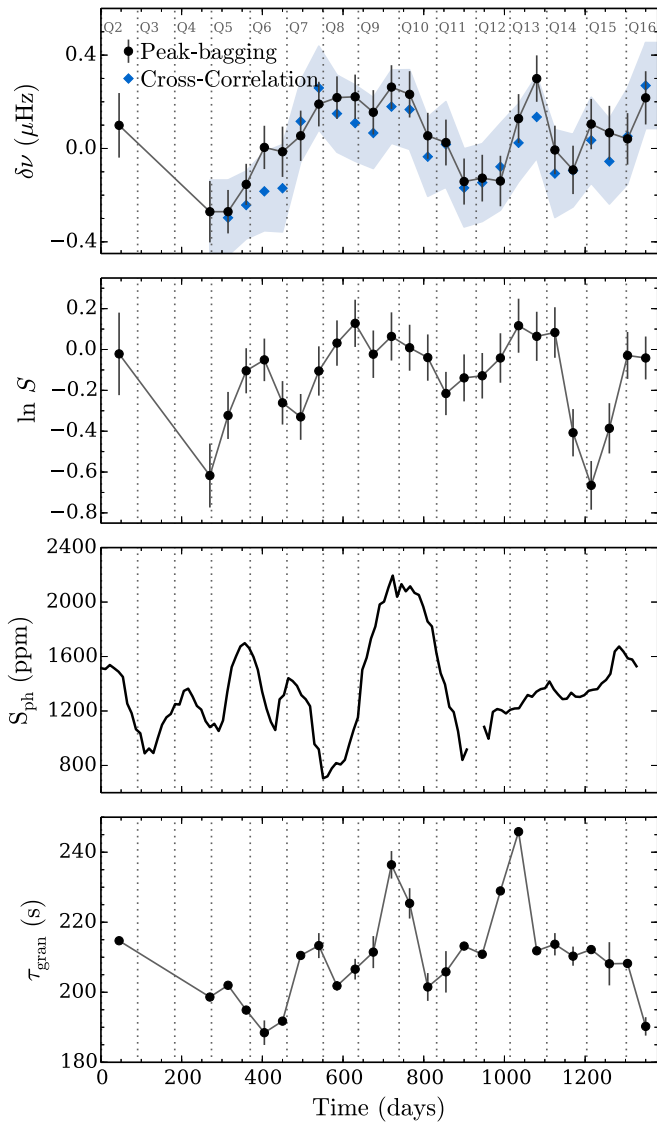

Figure 8. Results for KIC 9414417 (same as in Figure 5): mean frequency shifts, mode heights, photometric activity proxy, and characteristic granulation timescale.

the cross-correlation method (blue symbols). The mode heights (second panel) do not show a significant variation over time, but their overall behavior suggests a decrease. This is confirmed by the results from the CCF (Table 3), which, despite the low significance, suggest an anti-correlation between frequency shifts and mode heights. The photometric activity proxy (third panel of Figure 10) shows an increase on the magnetic activity, consistent with the rising phase of a cycle and consistent with the variation in the frequency shifts. The CCF results (Table 3) indicates that the frequency shifts and S_{ph} are correlated.

The variation in the characteristic timescale of the granulation is not consistent with the variation in the frequency shifts (bottom panel of Figure 10).

3.3.5. KIC 8379927

The black symbols in the top panel of Figure 11 show the mean frequency shifts for KIC 8379927 obtained from the peak-bagging analysis, which are in good agreement with those from the cross-correlation method (blue). The

logarithmic mode heights are shown in the second panel of Figure 11 and vary approximately in phase with the frequency shifts (opposite behavior to the solar case). This is confirmed by the CCF (Table 3), which shows that the frequency shifts and mode heights are correlated. The photometric activity proxy (third panel of Figure 11) suggests a relatively strong photometric activity for this star. The variation in the S_{ph} index is consistent with that in the frequency shifts. However, the correlation between the frequency shifts and S_{ph} is below the 95% significance level (Table 3). The granulation timescale for KIC 8379927 is shown in the bottom panel of Figure 11. The CCF results suggest a correlation between frequency shifts and granulation timescale.

KIC 8379927 is a known spectroscopic binary, thus one must be cautious before drawing further conclusions. Nevertheless, both frequency shifts and photometric activity proxy are observed to vary over time, and it would be interesting to understand if there is any connection between those variations and the properties of the binary.
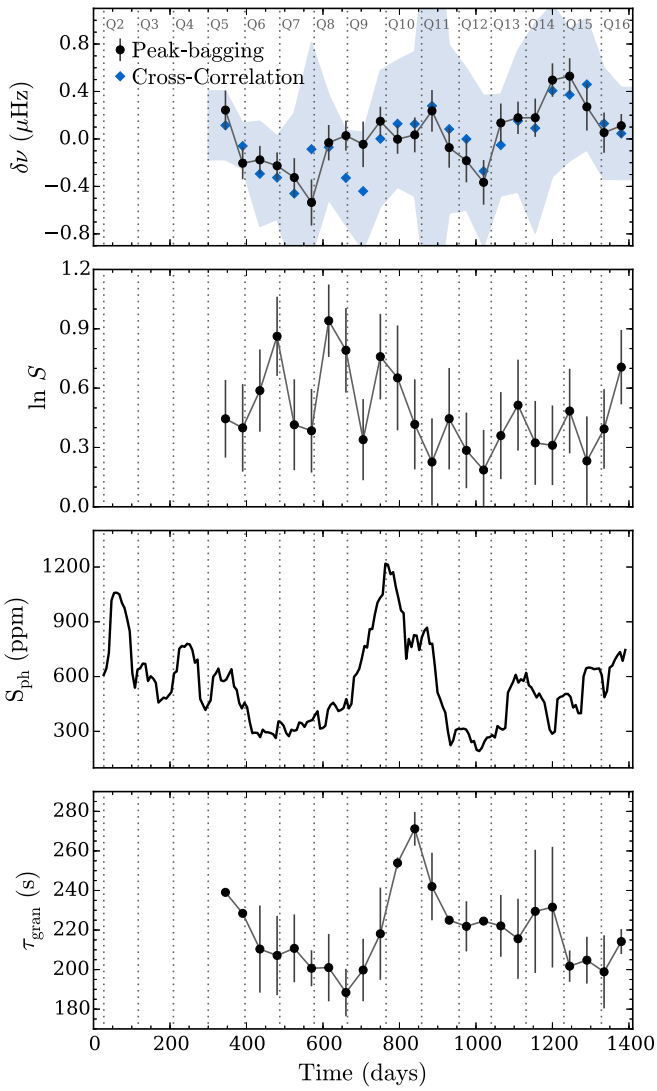
Figure 9. Results for KIC 10644253 (same as in Figure 5): mean frequency shifts, mode heights, photometric activity proxy, and characteristic granulation timescale.

Figure 10. Results for KIC 7970740 (same as in Figure 5): mean frequency shifts, mode heights, photometric activity proxy, and characteristic granulation timescale.

4. Summary and Discussion

In this work, we analyzed a large sample of solar-type stars observed by *Kepler* in order to search for temporal variations in the frequencies of the acoustic modes, which could possibly be related to magnetic activity.

The original data sets were split into 90-day sub-series (with 50% overlap) for which we modeled the power-density spectra. In order to obtain accurate individual mode parameters, we developed a Bayesian peak-bagging tool. With the individual mode frequencies in hand, we computed the mean frequency shifts for each star.

The method was first validated with observational and artificial solar data and then applied to the *Kepler* targets. To further confirm the efficiency of our peak-bagging tool, we compared the mean frequency shifts with those obtained with the cross-correlation method described in Kiefer et al. (2017). The results from the peak-bagging analysis and from the cross-correlation method are generally in good agreement. In addition, the error bars associated with the Bayesian peak-bagging

analysis are smaller than those associated with the cross-correlation method.

In order to connect the variation in the acoustic frequencies to an activity-related origin, the mean frequency shifts were compared with the mean logarithmic mode height, with the granulation timescale, and with the photometric activity proxy, S_{ph}.

More than half of the target sample shows evidence for periodic variations in the acoustic frequencies. For some of those stars, we also found consistent variations in the other parameters. In particular, we highlighted the results for five stars: KIC 8006161, KIC 5184732, KIC 9414417, KIC 10644253, KIC 7970740, and KIC 8379927.

For KIC 8006161, KIC 5184732, and KIC 7970740, the variations in the acoustic frequencies are consistent with the S_{ph} index and anti-correlated with the variations in the mode heights. These results resemble what is observed for the Sun: the frequency shifts vary in phase with the activity level, while the mode heights vary in anti-phase. Although the seismic

Figure 11. Results for KIC 8379927 (same as in Figure 5): mean frequency shifts, mode heights, photometric activity proxy, and characteristic granulation timescale.

properties for KIC 8006161 show a similar behavior to the solar parameters, its magnetic activity cycle is significantly stronger than the solar cycle (for a detailed study of KIC 8006161, see Karoff et al. 2018).

For KIC 10644253, the temporal frequency shifts are accompanied by variations in the S_{ph} index and in the granulation characteristic timescale.

For KIC 9414417 and KIC 8379927 (known spectroscopic binary), the frequency shifts are consistent, being approximately in phase, with the variation in the photometric proxy and in the mode heights. The relation between the frequency shifts and mode heights is opposite to the expected behavior, based on solar observations. This behavior is found in ∼20% of the analyzed targets.

In Appendix B, we present the results for the remainder of the Kepler stars in the sample.

Taking advantage of high-quality long-term photometric time-series like those obtained by Kepler, the analysis and results of this large-scale work confirm the possibility of using asteroseismology to study stellar magnetism. A follow-up work

(A. R. G. Santos et al. 2018, in preparation) is being prepared, where, for the ensemble of solar-type stars (analyzed in the present work), we study the relation between the observed frequency shifts and the stellar fundamental properties, such as age, effective temperature, and surface rotation.

Appendix A
Validation of the Peak-bagging Tool

Before using the peak-bagging tool to search for temporal variations in the acoustic frequencies of Kepler targets, we performed validation tests with solar data. The following sections present the results obtained from the analysis of VIRGO/SPM (Variability of solar IRradiance and Gravity Oscillations on board SOlar and Heliospheric Observatory (SOHO), where SPM stands for sunphotometers; Fröhlich et al. 1995, 1997; Jiménez et al. 2002) data and artificial BiSON (Birmingham Solar-Oscillations Network) data.

A.1. VIRGO/SPM Data

The first validation test is performed with ∼12-year VIRGO/SPM time-series from the green channel. To estimate the temporal variations in the solar acoustic frequencies, the original light curve is divided into 90 days segments
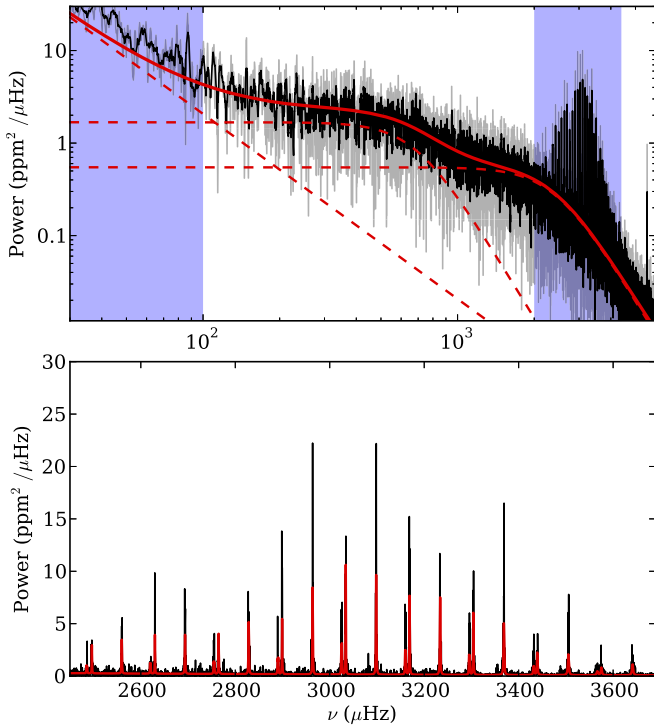
Figure 12. Solar power-density spectrum (black and gray) for a VIRGO/SPM sub-series of 90 days. The red solid lines show the best fits to the background signal (top panel) and to the p-modes (bottom panel; obtained with the peak-bagging tool). The dashed lines correspond to the different contributions to the brightness variability. The blue regions mark the frequency ranges neglected from the fitting process.

overlapped by 45 days (as performed for the analysis of *Kepler* targets).

In the case of VIRGO/SPM data, the background model also includes a facular component with characteristic timescale fixed at the value 65.8 s (Karoff 2012). The top panel in Figure 12 compares the solar power spectrum, for a given segment, with the background model that best fits the data.

Having the background model for each sub-series, we apply the peak-bagging tool (Section 2.5) to perform the global fit to the acoustic modes. The prior functions were defined as described in Section 2.5.1, with exception of those for the rotational splitting and inclination angle:

1. *Rotational splitting*. We use a uniform prior between 0 and 5 μHz.
2. *Inclination angle*. In order to avoid boundary effects in the sampling (e.g., Lund et al. 2014, 2017; Campante et al. 2016), the inclination is sampled from a uniform prior within $-90°$ to $180°$ and then folded onto the range $[0°, 90°]$.

The values ν_{nl}^0 are taken from Stahn (2010, for VIRGO/SPM data) and Broomhall et al. (2009, for BiSON data).

The bottom panel of Figure 12 shows the best fit to the solar acoustic modes. The corresponding parameters are estimated from the corresponding posterior distributions as described in Section 2.5.2.

With the frequencies of the acoustic modes in hand, we then compute the observed frequency shifts. We follow the procedure described in Section 2.6 with the only difference being the the inertia ratio (Q_{nl}; Christensen-Dalsgaard & Berthomieu 1991), which is not neglected in the solar
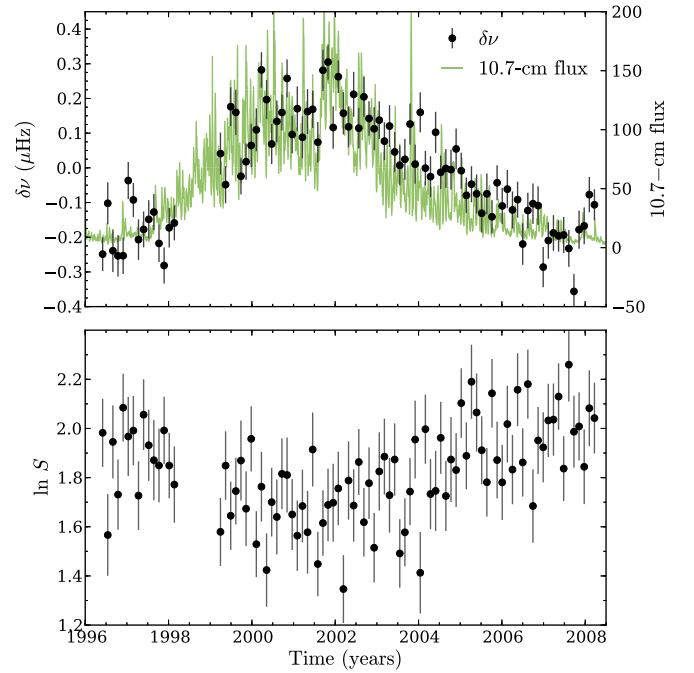
Figure 13. Mean frequency shifts (black; top) and logarithmic mode heights (bottom) obtained from the peak-bagging analysis of the VIRGO/SPM data. For comparison, the daily values of the 10.7 cm flux are shown in top panel in light green. The time interval between 1998 and 1999 corresponds to the so-called *SOHO* vacations (Appourchaux 2005).

case, i.e., we estimate the mean frequency shifts and the respective uncertainties as (Chaplin et al. 2007; Tripathy et al. 2007)

$$\delta\nu(t) = \frac{\sum_{nl} Q_{nl}\delta\nu_{nl}(t)/\sigma_{nl}^2(t)}{\sum_{nl} Q_{nl}/\sigma_{nl}^2(t)}, \qquad (18)$$

$$\sigma(t) = \left(\sum_{nl} \frac{Q_{nl}}{\sigma_{nl}^2(t)}\right)^{-1/2}. \qquad (19)$$

The top panel of Figure 13 shows the good agreement between the behavior of the frequency shifts over solar cycle 23 and the 10.7 cm flux (from NOAA/NGDC[11]—National Geophysical Data Center, part of the National Oceanic and Atmospheric Administration). These results are also consistent with those in the literature (e.g., Chaplin et al. 2007; Tripathy et al. 2007, 2011; Jain et al. 2009). This shows that the peak-bagging tool is able to successfully recover the time behavior of the solar acoustic frequencies.

The bottom panel of Figure 13 shows the evolution of the weighted average of the logarithmic mode heights obtained with the peak-bagging tool. As expected, the mode heights show a behavior opposite to that of the frequencies and decrease towards the solar maximum.

Figure 14 shows the frequency shifts for the individual angular degrees as a function of the observed 10.7 cm flux and the respective best linear fit (note that, as a first approximation, we neglect the magnetic hysteresis). The slope or shift gradient corresponds to the frequency shift per unit change in activity and is shown in Figure 15. Our results are consistent with those from Chaplin et al. (2004). For

---

[11] http://www.ngdc.noaa.gov
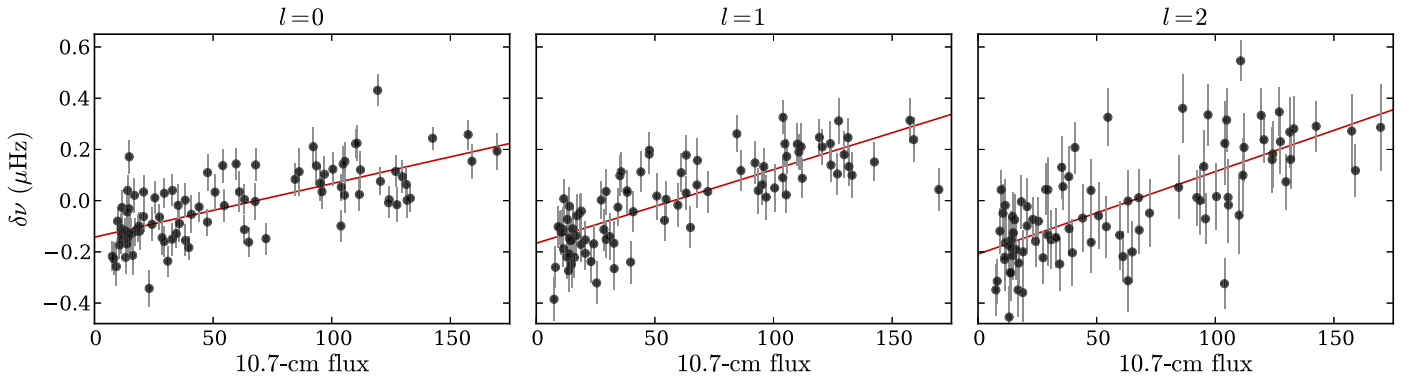
Figure 14. Frequency shifts for the VIRGO/SPM data as a function of the 10.7 cm flux for the individual angular degrees: $l = 0$, $l = 1$, and $l = 2$ (from left to right). The black solid line, the red dotted line, and the blue dashed line show the respective best linear fits.
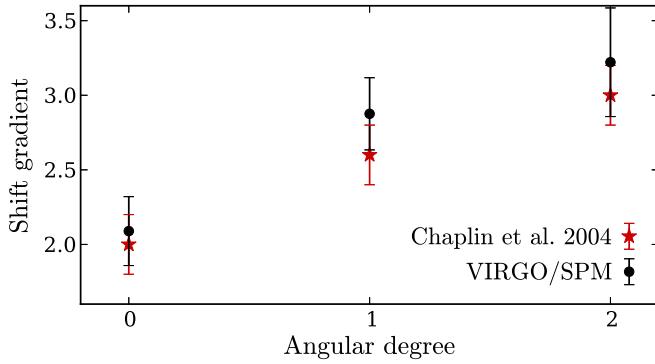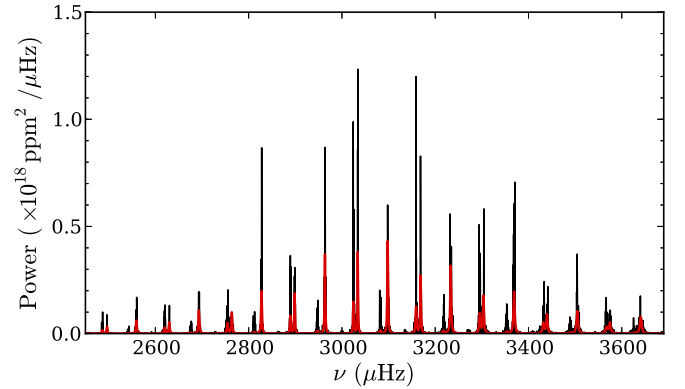

Figure 15. Frequency shift per unit change in activity, shift gradient (black), as a function of the angular degree for VIRGO/SPM data. For comparison, the red stars indicate the values found by Chaplin et al. (2004).

Figure 16. Power-density spectrum (black) for a 90-day sub-series for the artificial BiSON time-series. The red line shows the best fit to the p-modes obtained with the peak-bagging tool.

low-degree modes ($l \leqslant 3$), the most important contribution for the degree dependence of the frequency shifts is the latitudinal distribution of the surface magnetic field. Thus, modes that are more sensitive to the low latitudes show larger frequency shifts (e.g., Chaplin et al. 2004; Broomhall et al. 2012; Salabert et al. 2015).

A.2. Artificial BiSON Data

The efficiency of the peak-bagging tool was also tested with an artificial BiSON data set that is used as control test. The artificial data simulate the granulation component, the acoustic oscillations (affected by the solar activity), and the photon shot-noise.

Similar to the previous section, the original time-series is split in 90 days segments overlapped by 45 days. Following the same procedure as in Appendix A.1 and assuming the respective background model (that accounts only for the granulation and noise components), we peak-bag the power-density spectra obtained from each sub-series. Figure 16 shows the best fit to the p-modes for a given segment of the synthetic data set. Then, we compute the temporal variations in the acoustic frequencies and mode heights and compare them with the input activity level (Figures 17–19). These results further confirm that our peak-bagging tool is able to successfully recover the magnetic signature on the seismic data.

Figure 17. Average frequency shifts (black; top) and logarithmic mode heights (bottom) obtained from the artificial BiSON time-series using our peak-bagging tool. For comparison, the input 10.7 cm flux is shown in green in the top panel.
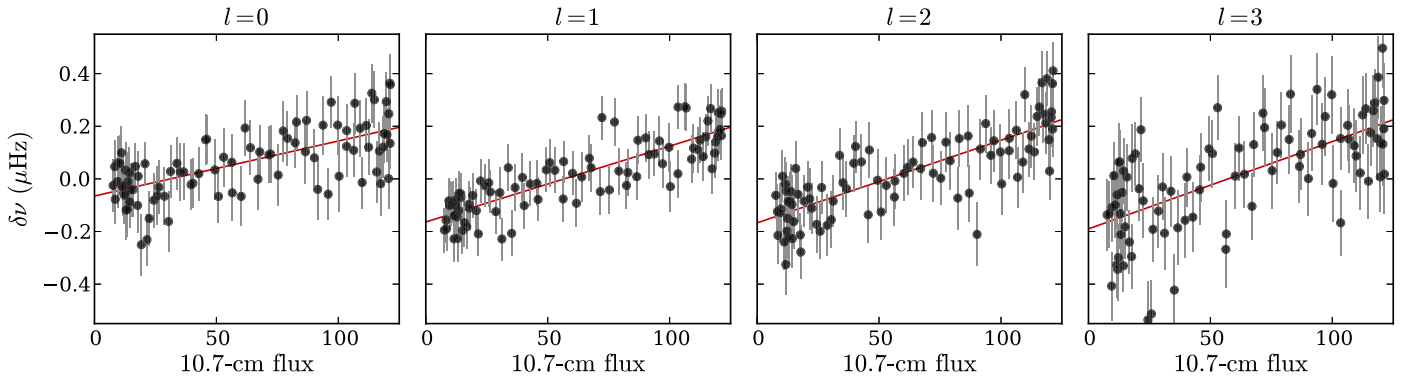
Figure 18. Frequency shifts for artificial BiSON data (black) as a function of the input 10.7 cm flux for the individual angular degrees: $l = 0$, $l = 1$, $l = 2$, and $l = 3$ (from left to right). The red lines show the best fits to the data.
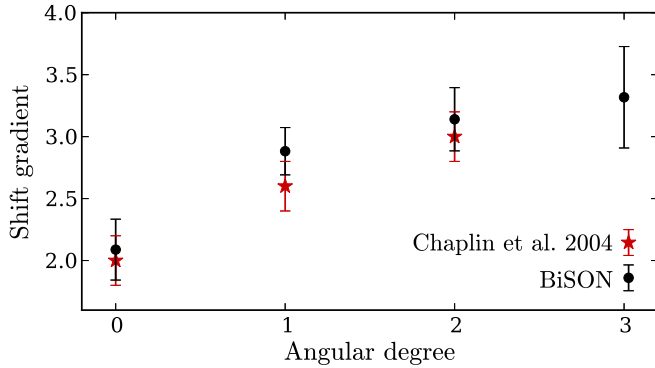

Figure 19. Frequency shift per unit change in activity, shift gradient, as a function of the angular degree for artificial BiSON data (black). The red stars show the shift gradients found by Chaplin et al. (2004).

Appendix B
Peak-bagging Analysis

This appendix presents the results for the *Kepler* stars in the sample: figures (Figure 20) and tables (in a machine readable format) available in the online journal. The results (both figures and table) for KIC 8006161 are shown in the main text, as well as the figures for KIC 5184732, KIC 7970740, KIC 8379927, KIC 9414417, and KIC 10644253. Note that for a number of stars it is not possible to measure the photometric activity proxy S_{ph}. Due to the large error bars and for representation purpose, for some stars we show the frequency shifts from the cross-correlation method were obtained with 180-day sub-series. Those cases are indicated.

In order to measure the correlation between the different quantities, we compute the CCF between frequency shifts and logarithmic mode heights, frequency shifts and interpolated photometric activity proxy, and frequency shifts and characteristic granulation timescale. In Table 3, we consider up to a temporal lag of ±90 days. We list the maximum absolute cross-correlation value and the corresponding lag. For reference, the 95% significance level is shown in the last column.
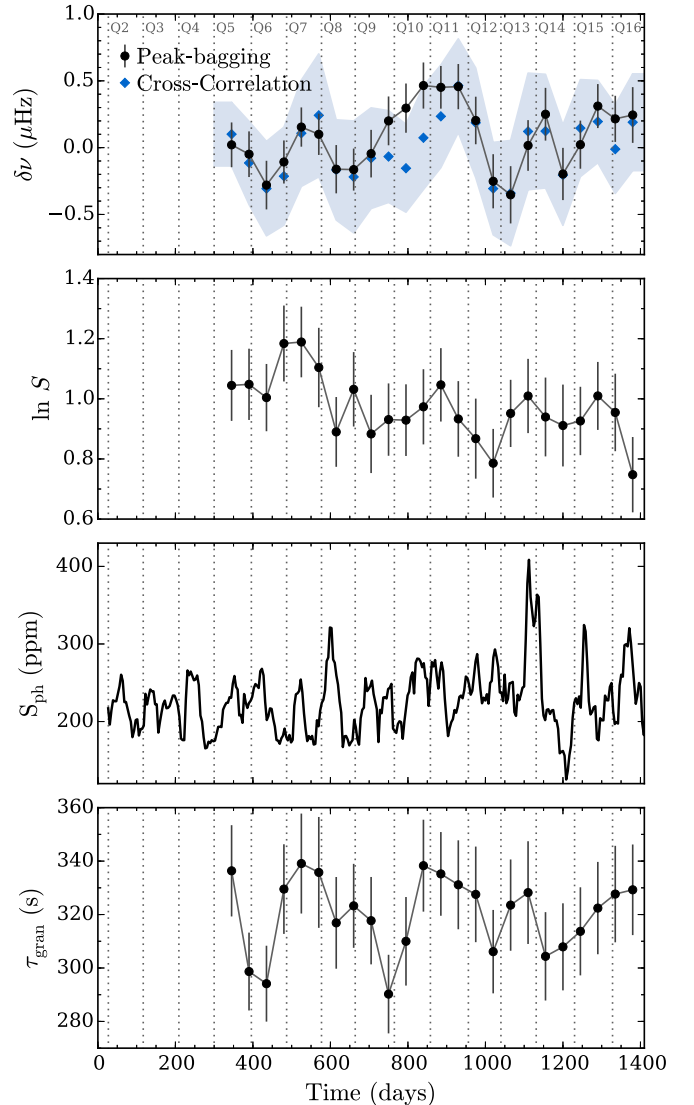
Figure 20. Same as in Figure 5, but for KIC 1435467. From top to bottom, time-dependent mean frequency shifts, mode heights, photometric activity proxy, and characteristic granulation timescale.

(The complete figure set (81 images) is available.)

ORCID iDs

A. R. G. Santos ⬤ https://orcid.org/0000-0001-7195-6542
T. L. Campante ⬤ https://orcid.org/0000-0002-4588-5389
W. J. Chaplin ⬤ https://orcid.org/0000-0002-5714-8618
M. S. Cunha ⬤ https://orcid.org/0000-0001-8237-7343
M. N. Lund ⬤ https://orcid.org/0000-0001-9214-5642
R. Kiefer ⬤ https://orcid.org/0000-0003-4166-5343
D. Salabert ⬤ https://orcid.org/0000-0002-0759-349X
G. R. Davies ⬤ https://orcid.org/0000-0002-4290-7351
R. Howe ⬤ https://orcid.org/0000-0002-3834-8585

References

Anderson, E. R., Duvall, T. L., Jr., & Jefferies, S. M. 1990, ApJ, 364, 699
Appourchaux, T. 2005, in Payload and Mission Definition in Space Sciences, ed. V. Martínez Pillet, A. Aparicio, & F. Sánchez (Cambridge: Cambridge Univ. Press), 185
Appourchaux, T., Gizon, L., & Rabello-Soares, M.-C. 1998, A&AS, 132, 107
Baglin, A., Auvergne, M., Barge, P., et al. 2006, ESA, 1306, 33
Baliunas, S. L., Donahue, R. A., Soon, W. H., et al. 1995, ApJ, 438, 269
Bazilevskaya, G., Broomhall, A.-M., Elsworth, Y., & Nakariakov, V. M. 2014, SSRv, 186, 359
Benomar, O., Appourchaux, T., & Baudin, F. 2009, A&A, 506, 15
Borucki, W. J., Koch, D., Basri, G., et al. 2010, Sci, 327, 977
Broomhall, A.-M., Chaplin, W. J., Davies, G. R., et al. 2009, MNRAS, 396, L100
Broomhall, A.-M., Chaplin, W. J., Elsworth, Y., & Simoniello, R. 2012, MNRAS, 420, 1405
Broomhall, A.-M., & Nakariakov, V. M. 2015, SoPh, 290, 3095
Brun, A. S., & Browning, M. K. 2017, LRSP, 14, 4
Campante, T. L., Handberg, R., Mathur, S., et al. 2011, A&A, 534, A6
Campante, T. L., Lund, M. N., Kuszlewicz, J. S., et al. 2016, ApJ, 819, 85
Casagrande, L., Silva Aguirre, V., Stello, D., et al. 2014, ApJ, 787, 110
Ceillier, T., van Saders, J., García, R. A., et al. 2016, MNRAS, 456, 119
Chaplin, W. J., Basu, S., Huber, D., et al. 2014, ApJS, 210, 1
Chaplin, W. J., Elsworth, Y., Isaak, G. R., et al. 1998, MNRAS, 300, 1077
Chaplin, W. J., Elsworth, Y., Isaak, G. R., Miller, B. A., & New, R. 2000, MNRAS, 313, 32
Chaplin, W. J., Elsworth, Y., Isaak, G. R., Miller, B. A., & New, R. 2004, MNRAS, 352, 1102
Chaplin, W. J., Elsworth, Y., Miller, B. A., Verner, G. A., & New, R. 2007, ApJ, 659, 1749
Chaplin, W. J., Kjeldsen, H., Bedding, T. R., et al. 2011, ApJ, 732, 54
Christensen-Dalsgaard, J., & Berthomieu, G. 1991, in Solar Interior and Atmosphere, ed. A. N. Cox, W. C. Livingston, & M. Mathews (Tucson, AZ: Univ. Arizona Press), 401
Davies, G. R., Chaplin, W. J., Farr, W. M., et al. 2015, MNRAS, 446, 2959
Davies, G. R., Silva Aguirre, V., Bedding, T. R., et al. 2016, MNRAS, 456, 2183
Dumusque, X., Bonomo, A. S., Haywood, R. D., et al. 2014, ApJ, 789, 154
Duvall, T. L., Jr., & Harvey, J. W. 1986, in Proc. NATO Advanced Research Workshop 169, Seismology of the sun and the distant stars (Dordrecht: Reidel), 105
Earl, D. J., & Deem, M. W. 2005, PCCP, 7, 3910
Egeland, R., Metcalfe, T. S., Hall, J. C., & Henry, G. W. 2015, ApJ, 812, 12
Elsworth, Y., Howe, R., Isaak, G. R., et al. 1993, MNRAS, 265, 888
Elsworth, Y., Howe, R., Isaak, G. R., McLeod, C. P., & New, R. 1990, Natur, 345, 322
Fletcher, S. T., Broomhall, A.-M., Salabert, D., et al. 2010, ApJL, 718, L19
Flores, M. G., Buccino, A. P., Saffe, C. E., & Mauas, P. J. D. 2017, MNRAS, 464, 4299
Foreman-Mackey, D., Hogg, D. W., Lang, D., & Goodman, J. 2013, PASP, 125, 306
Fröhlich, C., Andersen, B. N., Appourchaux, T., et al. 1997, SoPh, 170, 1
Fröhlich, C., Romero, J., Roth, H., et al. 1995, SoPh, 162, 101
Gabriel, M. 1994, A&A, 292, 281
García, R. A., Ceillier, T., Salabert, D., et al. 2014, A&A, 572, A34
García, R. A., Hekker, S., Stello, D., et al. 2011, MNRAS, 414, L6
García, R. A., Mathur, S., Salabert, D., et al. 2010, Sci, 329, 1032
García, R. A., Régulo, C., Samadi, R., et al. 2009, A&A, 506, 41
Gizon, L., & Solanki, S. K. 2003, ApJ, 589, 1009

Goldreich, P., & Keeley, D. A. 1977, ApJ, 212, 243
Goodman, J., & Weare, J. 2010, Comm. App. Math. and Comp. Sci., 5, 65
Handberg, R., & Campante, T. L. 2011, A&A, 527, A56
Handberg, R., & Lund, M. N. 2014, MNRAS, 445, 2698
Harvey, J. 1985, in Future Missions in Solar, Heliospheric & Space Plasma Physics, Vol. 235 ed. E. Rolfe & B. Battrick (Noordwijk: ESA), 199
Howe, R., Davies, G. R., Chaplin, W. J., Elsworth, Y. P., & Hale, S. J. 2015, MNRAS, 454, 4120
Huber, D., Bedding, T. R., Stello, D., et al. 2011, ApJ, 743, 143
Huber, D., Chaplin, W. J., Christensen-Dalsgaard, J., et al. 2013, ApJ, 767, 127
Huber, D., Stello, D., Bedding, T. R., et al. 2009, CoAst, 160, 74
Jain, K., Tripathy, S. C., & Hill, F. 2009, ApJ, 695, 1567
Jiménez, A., Roca Cortés, T., & Jiménez-Reyes, S. J. 2002, SoPh, 209, 247
Jiménez-Reyes, S. J., Régulo, C., Pallé, P. L., & Roca Cortes, T. 1998, A&A, 329, 1119
Kallinger, T., De Ridder, J., Hekker, S., et al. 2014, A&A, 570, A41
Kallinger, T., & Matthews, J. M. 2010, ApJL, 711, L35
Karoff, C. 2012, MNRAS, 421, 3170
Karoff, C., Campante, T. L., Ballot, J., et al. 2013a, ApJ, 767, 34
Karoff, C., Metcalfe, T. S., Chaplin, W. J., et al. 2013b, MNRAS, 433, 3227
Karoff, C., Metcalfe, T. S., Santos, A. R. G., et al. 2018, ApJ, 852, 46
Kiefer, R., Schad, A., Davies, G., & Roth, M. 2017, A&A, 598, A77
Kjeldsen, H., & Bedding, T. R. 2011, A&A, 529, L8
Lefebvre, S., García, R. A., Jiménez-Reyes, S. J., Turck-Chièze, S., & Mathur, S. 2008, A&A, 490, 1143
Libbrecht, K. G., & Woodard, M. F. 1990, Natur, 345, 779
Lund, M. N., Lundkvist, M., Silva Aguirre, V., et al. 2014, A&A, 570, A54
Lund, M. N., Silva Aguirre, V., Davies, G. R., et al. 2017, ApJ, 835, 172
Mathur, S., García, R. A., Ballot, J., et al. 2014, A&A, 562, A124
Mathur, S., Hekker, S., Trampedach, R., et al. 2011, ApJ, 741, 119
McIntosh, S. W., Leamon, R. J., Krista, L. D., et al. 2015, NatCo, 6, 6491
McQuillan, A., Mazeh, T., & Aigrain, S. 2013, ApJL, 775, L11
McQuillan, A., Mazeh, T., & Aigrain, S. 2014, ApJS, 211, 24
Metcalfe, T. S., Basu, S., Henry, T. J., et al. 2010, ApJL, 723, L213
Metcalfe, T. S., Buccino, A. P., Brown, B. P., et al. 2013, ApJL, 763, L26
Moreno-Insertis, F., & Solanki, S. K. 2000, MNRAS, 313, 411
Muller, R., Hanslmeier, A., & Saldaña-Muñoz, M. 2007, A&A, 475, 717
Oláh, K., Kolláth, Z., Granzer, T., et al. 2009, A&A, 501, 703
Pallé, P. L., Jiménez, A., Perez Hernandez, F., et al. 1995, ApJ, 441, 952
Paxton, B., Bildsten, L., Dotter, A., et al. 2011, ApJS, 192, 3
Paxton, B., Cantiello, M., Arras, P., et al. 2013, ApJS, 208, 4
Pinsonneault, M. H., An, D., Molenda-Żakowicz, J., et al. 2012, ApJS, 199, 30
Pinsonneault, M. H., Elsworth, Y., Epstein, C., et al. 2014, ApJS, 215, 19
Ramírez, I., Meléndez, J., & Asplund, M. 2009, A&A, 508, L17
Régulo, C., García, R. A., & Ballot, J. 2016, A&A, 589, A103
Régulo, C., Roca Cortés, T., & Vázquez Ramió, H. 2002, ESA, 506, 889
Régulo, C., Vázquez Ramió, H., & Roca Cortés, T. 2005, A&A, 443, 1013
Salabert, D., García, R. A., Beck, P. G., et al. 2016a, A&A, 596, A31
Salabert, D., García, R. A., Jiménez, A., et al. 2017, A&A, 608, A87
Salabert, D., García, R. A., Pallé, P. L., & Jiménez-Reyes, S. J. 2009, A&A, 504, L1
Salabert, D., García, R. A., & Turck-Chièze, S. 2015, A&A, 578, A137
Salabert, D., & Jiménez-Reyes, S. J. 2006, ApJ, 650, 451
Salabert, D., Régulo, C., García, R. A., et al. 2016b, A&A, 589, A118
Salabert, D., Régulo, C., Pérez Hernández, F., & García, R. A. 2018, A&A, 611, A84
Santos, A. R. G., Cunha, M. S., Avelino, P. P., Chaplin, W. J., & Campante, T. L. 2016, MNRAS, 461, 224
Santos, A. R. G., Cunha, M. S., Avelino, P. P., Chaplin, W. J., & Campante, T. L. 2017, MNRAS, 464, 4408
Silva Aguirre, V., Davies, G. R., Basu, S., et al. 2015, MNRAS, 452, 2127
Silva Aguirre, V., Lund, M. N., Antia, H. M., et al. 2017, ApJ, 835, 173
Simoniello, R., Finsterle, W., Salabert, D., et al. 2012, A&A, 539, A135
Simoniello, R., Jain, K., Tripathy, S. C., et al. 2013, ApJ, 765, 100
Smith, J. C., Stumpe, M. C., Van Cleve, J. E., et al. 2012, PASP, 124, 1000
Stahn, T. 2010, PhD thesis, Mathematisch-Naturwissenschaftlichen Fakultäten der Georg-August-Universität zu Göttingen
Stumpe, M. C., Smith, J. C., Van Cleve, J. E., et al. 2012, PASP, 124, 985
Toutain, T., & Appourchaux, T. 1994, A&A, 289, 649
Tripathy, S. C., Hill, F., Jain, K., & Leibacher, J. W. 2007, SoPh, 243, 105
Tripathy, S. C., Jain, K., Salabert, D., et al. 2011, J. Phys. Conf. Ser., 271, 012055
Walkowicz, L. M., & Basri, G. S. 2013, MNRAS, 436, 1883
Wilson, O. C. 1978, ApJ, 226, 379
Woodard, M. F., & Noyes, R. W. 1985, Natur, 318, 449